JOURNAL OF PROPULSION AND POWER
Vol. 38, No. 4, July–August 2022

Nonequilibrium Effects in Hypersonic Combustion Modeling

Wei Yao*
Institute of Mechanics, Chinese Academy of Sciences, 100190 Beijing, People's Republic of China

https://doi.org/10.2514/1.B38617

A zonal nonequilibrium model (ZNM) based on the concept of zonal representation of the nonequilibrium relaxation times is proposed. ZNM, together with dynamic zone flamelet model, zonal dynamic adaptive chemistry, and zonal in situ adaptive tabulation, forms the complete framework for nonequilibrium combustion modeling. The framework is then applied to the modeling of a high-*Ma* scramjet operating at Mach 12 based on improved delayed detached eddy simulation with a total of 92.52 million cells. The nonequilibrium effects exerted noticeable influences on the flow characteristics and engine performance through two main mechanisms, i.e., cooling and radical farming. Under a reduced flame temperature, the mixing efficiency increases due to the lower viscosity, whereas both the combustion efficiency and thrust recede. The Borghi diagram incorporating the compressibility effect shows that nearly 2/3 of the zones are in the flamelet mode, and the flamelet mode distributes wider under nonequilibrium.

Nomenclature

A	=	Arrhenius rate constant, $\mathrm{cm}^3/(\mathrm{mol}\cdot\mathrm{s})$
A_s	=	species-related coefficient for vibrational–translational relaxation time model
B_s	=	species-related coefficient for vibrational–translational relaxation time model
C_p	=	specific heat at constant pressure, $\mathrm{J}/(\mathrm{kg}\cdot\mathrm{K})$
c	=	a second conditional variable
D'	=	dissociation energy, J/kg
Da	=	Damköhler number
D_α, D_ξ	=	mass diffusivities of species α and mixture fraction ξ, m^2/s
d_{IDDES}	=	length scale in improved delayed detached eddy simulation, m
e_{el}	=	electronic energy, J/kg
F_{bx}	=	streamwise force, N
H, H^0, H_t	=	absolute enthalpy, formation enthalpy, and total absolute enthalpy, J/kg
$H_{\mathrm{tr}}, H_{\mathrm{vel}}$	=	trans-rotational and vibrational-electron-electronic energy, J/kg
H_0	=	stagnation enthalpy, MJ/kg
I	=	streamwise momentum flux, N
K_a	=	Karlovitz number
K_{eq}	=	equilibrium constant of chemical reaction
k_{res}	=	turbulent kinetic energy of the resolved motions, $\mathrm{m}^2/\mathrm{s}^2$
k_{sgs}	=	unresolved turbulent kinetic energy, $\mathrm{m}^2/\mathrm{s}^2$
L, M, N	=	numbers of species, reactions, and mesh cell
M_η	=	conditional diffusion
Ma	=	Mach number
Ma_s	=	subgrid Mach number
$\dot{m}$	=	mass flow rates, kg/s
$\dot{m}_p$	=	phase change rate, kg/s
n	=	number density, m^{-3}
$P(\eta)$	=	probability density function with the independent variable η
Pr_t	=	turbulent Prandtl number
p, P_t	=	static and total pressure, Pa
Q_T	=	conditionally averaged temperature, K
Q_{VT}	=	vibrational–translational energy exchange rate, W/m^3
Q_α	=	conditional mean of mass fraction for species α
Q'_α	=	conditional mean of mass fraction fluctuation for species α
q	=	dynamic pressure, kPa
R, R_u	=	gas constant $[\mathrm{J}/(\mathrm{kg}\cdot\mathrm{K})]$ and universal gas constant $[\approx 8.314\ \mathrm{J}/(\mathrm{mol}\cdot\mathrm{K})]$
Re	=	Reynolds number
S	=	cross-sectional area, m^2
S_{ij}	=	strain rate tensor, m/s
Sc_t	=	turbulent Schmidt number
T, T_0	=	static temperature and total temperature, K
T'	=	temperature fluctuation, K
T_a	=	activation temperature, K
$T_{c,b}$	=	control temperature of backward reactions, K
$T_{c,f}$	=	control temperature of forward reactions, K
T_p	=	Park's overall temperature, K
T_t, T_v	=	trans-rotational and vibrational-electron-electronic temperature, K
t	=	time, s
$\boldsymbol{U}$	=	velocity vector, m/s
u_i, u'_i	=	the ith-component of velocity and its fluctuation, m/s
V	=	cell volume, m^3
$W_m, W_{m,\alpha}$	=	molecular weight of mixture and species α, g/mol
W_α	=	production rate of species α, s^{-1}
X_α	=	molecular fraction of species α
x	=	streamwise distance, m
x_i	=	Cartesian coordinate in the ith direction
Y_α	=	mass fraction of species α
Y'_α	=	mass fraction fluctuation around the conditional mean for species α
$Y_{l,\alpha}$	=	mass fraction of species α in the liquid phase
y^+	=	nondimensional wall distance
α	=	species order
β	=	dimensionless temperature index in Arrhenius equation
Δ	=	local filter width of the subgrid turbulence, m
δ_{ij}	=	Kronecker delta function
ϵ	=	small quantity
ϵ	=	turbulence dissipation rate, $\mathrm{J}/(\mathrm{kg}\cdot\mathrm{s})$ or $\mathrm{m}^2/\mathrm{s}^3$
η	=	sample space for mixture fraction
θ	=	sample space for a second conditional variable
λ_e	=	chemical explosives mode index
ν, ν_{sgs}	=	kinematic viscosity and turbulent viscosity, m^2/s

Presented as Paper 2021-3543 at the AIAA Propulsion and Energy 2021 Forum, Virtual Event, August 9–11, 2021; received 17 August 2021; revision received 15 November 2021; accepted for publication 3 December 2021; published online 25 January 2022.

*Associate Professor, Key Laboratory of High-Temperature Gas Dynamics; also School of Engineering Science, University of Chinese Academy of Science, 100049 Beijing, People's Republic of China; weiyao@imech.ac.cn. Member AIAA (Corresponding Author).

ξ_{st} = stoichiometric mixture fraction
$\tilde{\xi}, \tilde{\xi''^2}$ = mean and variance of mixture fraction
ρ = density, kg/m^3
σ = model constant for vibrational–translational relaxation time model, 10^{-21} m^2
τ_c = time scale of chemical reactions, s
$\tilde{\tau}_{ij}, \tau_{ij}$ = viscous and Reynolds stress tensor, kg/(m · s^2)
τ_k = Kolmogorov time scale, s
τ_t = turbulence time scale, s
τ_{VT} = vibrational–translational relaxation time, s
Φ = global fuel equivalence ratio
$\tilde{\chi}$ = mean scalar dissipation rate, s^{-1}
$\Psi_{T,j}$ = turbulent enthalpy flux, W/m^2
$\Psi_{\xi,j}$ = turbulent species diffusion, kg/(m^2 · s)
ω_α = mass production of species α, kg/(m^3 · s)
$\dot{\omega}$ = reaction rate, kg/(m^3 · s)

Subscripts

inlet = inlet injection
combustor = combustor injection
i, j = different components of a vector
α = species index

Superscripts

$\sim$ = Favre-averaged quantity
$-$ = averaged quantity

I. Introduction

WITH the increase of flight altitude and Mach number (stagnation temperature), the complexity of physical and chemical processes in gas increases sharply, successively undergoing vibrational excitation and nonequilibrium chemistry (air dissociation and ionization). Under high Knudsen number, the role of thermal and chemical nonequilibrium effects emerges due to the lack of intermolecular collisions [1]. With the increase of stagnation temperature at higher Mach numbers, the vibrational modes of molecules will be excited, and various thermal/chemical nonequilibrium phenomena, such as dissociation and ionization, will occur. At standard atmospheric pressure, the vibrational energy mode is excited when the temperature is higher than 800 K; O_2 and N_2 begin to dissociate when the temperature is higher than 2500 and 4000 K, respectively, whereas ionization occurs at a higher temperature. The dissociation temperature decreases with pressure, implying that nonequilibrium chemistry is easier to occur at high altitudes. Although most aerospace vehicles and their integrated engines operate in the nonequilibrium range, the integrated modeling of nonequilibrium and combustion is generally rare in the literature, mainly due to the complexity of multiphysics coupling and the huge computational cost. Currently, most of the nonequilibrium flow modelings were applied only to the external flows, e.g., the reentry of space vehicles [2–4].

For airbreathing hypersonic vehicles with flight Mach numbers over 8, the nonequilibrium effects on the combustion need to be considered in the engine design and performance analysis. In a scramjet, the compression by forebody/inlet shock waves and the flow deceleration by frictional walls are responsible for the initialization of nonequilibrium. Air molecules can be dissociated or even ionized in the high-enthalpy postshock regions and boundary layers but usually have little chance to recombine due to the lack of intermolecular collisions given the short flow residence time. The vibrational–translational (V-T) energy exchange strongly relies on collisions [5]; thus, the status of vibrational excitation will be temporally frozen and carried downstream to the combustor, where the nonequilibrium may have a significant impact on the ignition, flame stabilization, and combustion efficiency. It was pointed out that [5,6], in addition to the direct influence of translational temperature on the reaction rates, the change in translational energy will affect the molecular viscosity and, in turn, the turbulent mixing of the fuel. The reduction in translational temperature retards the lamination of the shear layer when nonequilibrium effects are taken into account [7]. Han et al. [7] numerically analyzed the impacts of thermochemical nonequilibrium on the performance of a model scramjet without fuel injection, where the vibrational freezing phenomenon was observed in the combustor; i.e., the vibrational temperature is insensitive to the variation of translational temperature because of the relatively large vibrational relaxation time in comparison with the flow residence time. Fiévet et al. [6] analyzed the effect of thermal nonequilibrium on ignition in scramjet combustors, where a so-called temperature-inversion-driven flame stabilization was observed. Koo et al. [5] observed that the vibrational nonequilibrium leads to a delayed ignition and increase in liftoff distance. Because of the vast difference in the relaxation time scales of individual species, the slowly relaxed species provide a continuous source of nonequilibrium [5].

In addition to the aforementioned nonequilibrium effects, it would be more interesting to evaluate the influence of nonequilibrium on the scramjet performance, including the inlet capture rate, the combustion efficiency of the combustor, and the nozzle thrust. To enable the internal–external coupled flow modeling, the multiphysics coupling between the nonequilibrium model and the combustion model needs to be addressed first. This study aims to establish a zone-based modeling framework for nonequilibrium combustion and then use it to evaluate the nonequilibrium effects on the performance of a high-Mach scramjet. Using the rectangular-to-elliptical shape transition (REST) experiment [8–10] as the reference case, a full-scale scramjet with part of the external forebody will be modeled using highly resolved large-eddy simulation incorporating nonequilibrium models. The flow characteristics and engine performance will be analyzed to reveal the influencing mechanisms of nonequilibrium effects.

II. Physical Models and Numerical Methods

A. Governing Equations

The unsteady and three-dimensional Favre-averaged compressible reactive Navier–Stokes equations are solved for a set of conservative variables ($\overline{\rho}$, $\tilde{u}_i$, $\tilde{H}_t$, $\tilde{\xi}$) [11,12]:

$$\frac{\partial \overline{\rho}}{\partial t} + \frac{\partial \overline{\rho}\tilde{u}_j}{\partial x_j} = 0 \tag{1}$$

$$\frac{\partial \overline{\rho}\tilde{u}_i}{\partial t} + \frac{\partial \overline{\rho}\tilde{u}_j\tilde{u}_i}{\partial x_j} + \frac{\partial \overline{p}}{\partial x_i} - \frac{\partial \tilde{\tau}_{ij}}{\partial x_j} = -\frac{\partial \tau_{ij}}{\partial x_j} \tag{2}$$

$$\frac{\partial \overline{\rho}\tilde{H}_t}{\partial t} + \frac{\partial \overline{\rho}\tilde{u}_j\tilde{H}_t}{\partial x_j} - \frac{\partial}{\partial x_j}\left(\overline{\rho}D_T\frac{\partial \tilde{H}_t}{\partial x_j} + \sum_{\alpha=1}^{L}\overline{\rho}\,D_\alpha\frac{\partial \tilde{Y}_\alpha}{\partial x_j}\tilde{H}_\alpha\right) - \frac{\partial \overline{p}}{\partial t} - \frac{\partial \tilde{u}_j\tilde{\tau}_{ij}}{\partial x_j} = -\frac{\partial \Psi_{T,j}}{\partial x_j} \tag{3}$$

$$\frac{\partial \overline{\rho}\tilde{Y}_\alpha}{\partial t} + \frac{\partial \overline{\rho}\tilde{u}_j\tilde{Y}_\alpha}{\partial x_j} - \underbrace{\frac{\partial}{\partial x_j}\left(\overline{\rho}D_\alpha\frac{\partial \tilde{Y}_\alpha}{\partial x_j}\right) = -\frac{\partial \Psi\alpha, j}{\partial x_j}}_{\text{not solved}} \tag{4}$$

$$\frac{\partial \overline{\rho}\tilde{\xi}}{\partial t} + \frac{\partial \overline{\rho}\tilde{u}_j\tilde{\xi}}{\partial x_j} - \frac{\partial}{\partial x_j}\left(\overline{\rho}D_\alpha\frac{\partial \tilde{\xi}}{\partial x_j}\right) = -\frac{\partial \Psi_{\xi,j}}{\partial x_j} \tag{5}$$

$$\tilde{\xi''^2} = C_{\text{var}}\Delta^2\left(\frac{\partial \tilde{\xi}}{\partial x_j}\frac{\partial \tilde{\xi}}{\partial x_j}\right) \tag{6}$$

$$\rho_\eta\frac{\partial Q_\alpha}{\partial t} + \langle \rho u_j|\eta\rangle_{\text{zone}}\frac{\partial Q_\alpha}{\partial x_j} = \rho_\eta\frac{D_\alpha}{D_\xi}\langle\chi|\eta\rangle_{\text{zone}}\frac{\partial^2 Q_\alpha}{\partial \eta^2} + \rho_\eta\left(\frac{D_\alpha}{D_\xi} - 1\right)M_\eta\frac{\partial Q_\alpha}{\partial \eta} + \rho_\eta\langle W_\alpha|\eta\rangle \tag{7}$$

$$\overline{p} = \overline{\rho} R \tilde{T} = \overline{\rho}\left(R_u\left(\sum_{\alpha=1}^{L} Y_\alpha / W_{m,\alpha}\right)\right)\tilde{T} \tag{8}$$

$$\tilde{H}_t = \tilde{H} + \frac{1}{2}\tilde{u}_i\tilde{u}_i = \tilde{H}^0 + \int_0^T C_p \, \mathrm{d}T + \frac{1}{2}\tilde{u}_i\tilde{u}_i \tag{9}$$

Here the bar (−) and the tilde (∼) represent averaged and Favre-averaged quantities, respectively. The energy equation in enthalpy form is usually preferred for reacting systems because most of the chemical energies are expressed in enthalpy forms [13]. The mean mixture fraction $\tilde{\xi}$ and the mixture fraction variance $\tilde{\xi''^2}$ are obtained from Eq. (5) and the algebraic gradient model [14] of Eq. (6) to estimate the probability density function (PDF). Instead of solving the mean species transport Eq. (4) for $\tilde{Y}_\alpha$, the four-dimensional Eq. (7) for the conditionally averaged mass fraction is solved, as described in the following combustion model section.

According to the Stokes's hypothesis, which ignores the bulk viscosity, the shear-stress tensor for a Newtonian fluid is calculated as

$$\tilde{\tau}_{ij} = \overline{\rho}\nu(\tilde{T})\left(2\tilde{S}_{ij} - \frac{2}{3}\delta_{ij}\tilde{S}_{kk}\right) \tag{10}$$

where ν is a temperature-dependent kinetic viscosity, and the strain-rate tensor of the resolved scales is calculated as

$$\tilde{S}_{ij} = \frac{1}{2}\left(\frac{\partial\tilde{u}_i}{\partial x_j} + \frac{\partial\tilde{u}_j}{\partial x_i}\right) \tag{11}$$

The thermodiffusion (Soret effect), barodiffusion, and mass-driven diffusion of heat (Dufour effect), subgrid-scale (SGS) species diffusive flux, SGS energy diffusive flux, SGS viscous dissipation, and SGS fluctuation in the gas state are all ignored.

The turbulent Reynolds stresses τ_{ij} and turbulent fluxes $\Psi_{T,j}$ and $\Psi_{\alpha,j}$) in Eqs. (2–5) are unclosed and require specific modeling. The Reynolds stress defined as $\tau_{ij} = \overline{\rho}(u_i\tilde{u}_j - \tilde{u}_i\tilde{u}_j)$ is modeled by the Boussinesq eddy viscosity hypothesis, where the Reynolds stresses are proportional to $\tilde{S}_{ij}$,

$$\tau_{ij} = \underbrace{\left(\tau_{ij} - \frac{1}{3}\delta_{ij}\tau_{kk}\right)}_{\text{deviatoric}} + \underbrace{\frac{1}{3}\delta_{ij}\tau_{kk}}_{\text{isotropic}} = -\overline{\rho}\nu_{\text{sgs}}\left(2\tilde{S}_{ij} - \frac{2}{3}\delta_{ij}\tilde{S}_{kk}\right) + \frac{2}{3}\delta_{ij}k_{\text{sgs}} \tag{12}$$

Here ν_{sgs} is the eddy viscosity given by a specified turbulence model, and k_{sgs} is the unresolved turbulent kinetic energy.

The turbulent enthalpy flux term $\Psi_{T,j} = \overline{\rho}(u_j\tilde{H}_t - \tilde{u}_j\tilde{H}_t)$ is modeled by the gradient diffusion assumption as

$$\Psi_{T,j} = -2\overline{\rho}\frac{\nu_t}{Pr_t}\frac{\partial\tilde{H}_t}{\partial x_j} \tag{13}$$

where Pr_t is the turbulent Prandtl number. The turbulent diffusion term for mixture faction $\Psi_{\xi,j} = \overline{\rho}(\tilde{u_j\xi} - \tilde{u}_j\tilde{\xi})$ is also modeled using the gradient diffusion assumption as

$$\Psi_{\xi,j} = -2\overline{\rho}\frac{\nu_t}{Sc_t}\frac{\partial\tilde{\xi}}{\partial x_j} \tag{14}$$

where Sc_t is the turbulent Schmidt number. In this study, unity Prandtl and Schmidt numbers are assumed.

B. Zonal Nonequilibrium Model

To describe the thermal nonequilibrium flow, the two-temperature model [15,16] is applied by decomposing the internal energy into its elementary energy modes and then subgrouping the translational and rotational temperatures into a single trans-rotational temperature (denoted by T_t), and the electron, electronic energy, and vibrational energy modes into a single vibrational–electronic temperature (denoted by T_v). The translational, rotational, vibrational, electronic, and electron energy modes comprise the total energy. The regrouping is based on the observation that the combined modes have similar characteristic times of relaxation toward thermal equilibrium. The energy equation for T_v is solved by introducing source terms to quantify the energy redistributions between the trans-rotational energy mode and the vibrational-electronic energy mode (V-T). Landau–Teller equation [17] is used to estimate the V-T energy exchange rate as

$$Q_{\text{VT}} = \rho\frac{H_{\text{tr}} - H_{\text{vel}}}{\tau_{\text{VT}}} \tag{15}$$

where H_{tr} and H_{vel} are the trans-rotational and vibrational–electron–electronic energy, respectively, and τ_{VT} is the V-T relaxation time. A semi-empirical correlation proposed by Millikan and White [18] ($\tau_{\text{VT}}^{\text{MW}}$) and further corrected by Park [15] (τ_{VT}^{P}) is used to evaluate the V-T relaxation time:

$$\tau_{\text{VT}} = \tau_{\text{VT}}^{\text{MW}} + \tau_{\text{VT}}^{P} \tag{16}$$

The mixture-averaged V-T relaxation time is calculated from the value of individual species α weighted by the molecular fraction X_α,

$$\tau_{\text{VT}} = \frac{\sum X_\alpha}{\sum X_\alpha/\tau_{\text{VT},\alpha}} \tag{17}$$

More complicated modeling is treating the vibrational temperature of individual species independently, for example, the formulation proposed by Knab et al. [19] to account for vibrational–vibrational (V-V) energy redistribution among species. However, the V-V energy transfer plays only a secondary role in vibrational energy exchange [2]. The vibrational coupling between the dissociated air molecules (e.g., N_2, O_2, and NO) is known to be strong only if their vibrational temperatures are nearly identical [20]. Thus, the multivibrational energy exchange was not considered in this study, whereas a single vibrational temperature was used for all species. It was also observed that, when using the single-vibrational-temperature model, the vibrational relaxation time is dominated by nitrogen [6].

The translational–vibrational and vibrational–vibrational energy exchanges are then coupled with the chemistry. The same reversible Arrhenius formula as in thermal equilibrium is used to calculate the reaction rate but with a different controlling temperature that is a function of the vibrational and translational temperatures. In this study, the chemistry–vibration coupling is calculated by the Park T-Tv model [21], where the controlling temperatures of the forward and backward reactions depend on the type of the chemical reactions, as listed in Table 1. The Park's overall temperature [22] is given as

$$T_p = T_t^{0.7} \cdot T_v^{0.3} \tag{18}$$

The vibrational–electronic energy added or removed by chemical reactions is calculated as

$$Q_{\text{CV}} = \dot{\omega}(D' + e_{\text{el}}) \tag{19}$$

where e_{el} is the electronic energy and D' is the dissociation energy. A preferential model [23], which assumes that molecules are more

Table 1 Controlling temperature depending on the type of the chemical reaction

Reaction type	Forward, $T_{c,f}$	Backward, $T_{c,b}$
Dissociation	T_p	T_t
Exchange	T_t	T_t
Associative ionization	T_t	T_v
Electron impact ionization	T_v	T_v
Charge exchange	T_t	T_t

likely to dissociate at higher vibrational energy states, is used to calculate D' to be the dissociation potential scaled by a constant fraction of around 0.3.

A zonal nonequilibrium model (ZNM) is developed in this study to improve computational efficiency for the calculation of V-T relaxation time for individual species and the nonequilibrium chemistry. In ZNM, the flow domain is regrouped into a finite number of zones in terms of pressure, temperature, and mixture fraction to ensure that they have similar nonequilibrium relaxation times. By using the concept of zone conditional average, the zone conditional relaxation time is defined as

$$\langle \tau_{\mathrm{VT}} | \eta, \mathrm{zone} \rangle = \frac{101325}{\langle p \rangle_{\mathrm{zone}}} \exp(A_s(\langle T_t | \eta \rangle^{-1/3} - B_s) - 18.42) + \left(\sqrt{\frac{8R\langle T_t | \eta \rangle}{\pi}} \cdot \sigma \left(\frac{5000}{\langle T_t | \eta \rangle} \right)^2 \cdot n \right)^{-1} \tag{20}$$

The above relationship is defined for the mixture in a conditional space, and the mean relaxation time is given by PDF weighted integration:

$$\tau_{\mathrm{VT}} = \int \langle \tau_{\mathrm{VT}} | \eta, \mathrm{zone} \rangle P(\eta)\, \mathrm{d}\eta$$

Then the source terms for each vibrationally excited species α can be calculated as in Eq. (15) by using the mean relaxation time. The relaxation time for a mixture is defined as $\tau_{\mathrm{VT},m} = 1/\sum(X_\alpha/\tau_{\mathrm{VT},\alpha})$ with X_α the molar fraction.

C. Zonal Dynamic Adaptive Chemistry

Zonal dynamic adaptive chemistry (Z-DAC) based on adaptive zone division is used to improve the pertinence of adaptive chemistry with the local thermochemical environment. Dynamic adaptive chemistry (DAC) [24,25] applies different sets of skeletal mechanisms in different regions by freezing the reaction paths and species that have a weak influence on the target kinetic properties, e.g., ignition delay. The reaction mechanism applied locally is usually the subset of a detailed mechanism. It can be seen that the key to achieving an accurate yet efficient application of DAC is appropriately partitioning the computational cells into different groups according to their similarity in terms of temperature and concentrations of concerned species [26]. In Z-DAC, mixture fraction is selected to differentiate the mixture composition, and temperature is used to characterize the reaction activity. Pressure can be added to the zone division indices if pressure-dependent reactions are included. Because the reacting statuses with each zone change dynamically with time, the zone division needs to be updated dynamically with the time evolution of the flowfield. Because of the homogeneity of thermochemical states within each zone, smaller kinetic mechanisms can usually be reduced. Direct relation graph (DRG) method [27] coupled with error propagation method, i.e., the so-called DRGEP [28], is used for the on-the-fly mechanism reduction in Z-DAC. The DRG reduction is scheduled for every specific interval. Once the flow becomes quasi-steady, the thermochemical states within each zone become relatively stable, and the frequency of on-the-fly mechanism reduction can be further lessened, e.g., from every 100 steps in the flow development state to 300 steps in the quasi-steady stage.

D. Zonal In Situ Adaptive Tabulation

In this study, a strategy of zonal in situ adaptive tabulation (Z-ISAT) is developed to increase the successful-retrieval ratio while maintaining a smaller lookup table through clustering the thermochemical states within each zone. The traditional in situ adaptive tabulation (ISAT) method [29,30] usually requires excessive memory and too frequent table maintenance due to the fast-growing lookup table. In Z-ISAT, the flowfield is firstly divided into a finite number of dynamic zones according to local thermochemical state parameters, and then a separate ISAT table is built for each zone. In contrast to the traditional ISAT implementation with fixed zones but variable ISAT tables, Z-ISAT has dynamic zones but relatively stable ISAT tables that do not need rebuilding even when the zone partition changes. In virtue of the local homogeneity of thermochemical states within each zone, both the coverage ratio of the lookup table and the ratio of successful retrievals are improved, and the maintenance frequency of the ISAT table can be significantly alleviated. Compared with the fixed ISAT partition strategy, Z-ISAT is especially suitable for highly transient and spatially heterogeneous combustion fields. The Computational Fluid Dynamics (CFD) cells included in each zone need to be updated constantly to keep a strong association between the ISAT zone and the ISAT table. Because of such a strong association, the ISAT tables can be stored and reused for restarted modelings and cases with similar conditions.

A cloud-computation strategy for ISAT is further developed to improve the dynamic load balance (DLB) among parallel processors. The communication-free pure local processing (PLP) strategy [31] is more suitable for relatively stable combustion modeling. However, the supersonic combustion in scramjets is highly unsteady, and the transient reaction regions usually evolve in dramatic oscillation [32]. Supersonic combustion has a high Reynolds number, usually of the order of 10^5–10^7, suggesting a much wide range of turbulent fluctuation. Both the oscillation in reacting regions and the fluctuation in reactive scalars demand frequent maintenance of the ISAT table. The computational load for such ISTA table maintenance is especially higher in the combustor, but almost negligible for the inlet and nozzle with nearly frozen chemistry. The cloud computing strategy divides the local thermochemical states into two groups, i.e., those frequently accessed and temporary states. Only the former is stored in the local ISAT table, whereas the latter are redistributed to the rest idle nodes. The rule of redistribution is to ensure that each processor is assigned a pack with roughly the same number of thermochemical states. Here, the criterion of distinguishing a frequently accessed state is that the state node in ISAT has been called for more than five times. The packing and redistribution of temporary states consume bandwidth and communication time as well. Therefore, the master processor first draws a global redistribution map counting the number of temporary states sent out in each processor. Then direct processor-to-processor (P2P) data exchanges concerted by the redistribution map are used to avoid the traffic congestion of collective data movement (e.g., gather, scatter, and broadcast), rather than the traditional gather/scatter operations. The use of a global redistribution map saves the memory to collect the states in all processors and expedites the data exchange process. The cloud-computation strategy ensures a minimum ISAT table containing the most frequently used states, and thus with a high retrieval ratio, but also substantially moderates the load imbalance of chemistry solving in unsteady yet heterogenous supersonic combustion fields.

E. Zone-Based Combustion Model

To effectively decouple the flow and chemistry solving locally, dynamic zone flamelet model (DZFM) [33–36] is proposed based on the idea of homogenizing the local turbulence-influenced chemical status within each zone. DZFM introduces the concept of zone-based conditional mean as $Q_\alpha = \langle Y_\alpha | \eta = \xi(x,t), x \in \mathrm{zone} \rangle$, where η is the sampling variable in the mixture fraction space $\xi(x,t)$, x is the physical coordinate, and $x \in$ zone denotes that the conditionally average is restricted to the local zone. The relationship between the instantaneous mass fraction Y_α and the representative mass fraction Q_α is

$$Y_\alpha(x,t) = Q_\alpha(\eta = \xi(x,t), x \in \mathrm{zone}, t) + Y'_\alpha(x \in \mathrm{zone}, t) \tag{21}$$

here Y'_α represents the fluctuation of instantaneous value deviating from the conditional mean at the current mixture fraction $\xi(x,t)$. The conditional fluctuation is zero $Q'_\alpha = \langle Y'_\alpha | \eta, x \in \mathrm{zone} \rangle = 0$, and it yields that the zone averaged fluctuation is also zero $\langle Q'_\alpha \rangle_{\mathrm{zone}} = \int Q'_\alpha P(\eta)\, \mathrm{d}\eta = 0$, where $P(\eta)$ is the PDF of the distribution of instantaneous mixture fraction ξ within the zone. Ideally, we have $Y'_\alpha \to 0$; i.e., the flamelet perfectly represents the local reacting

status, which is the concept of representative interactive flamelets (RIFs) [37]. RIFs approximate the relationship between mixture fraction and thermochemical state [38], rather than pursuing an exact asymptotic relationship as in the steady laminar flamelet (SLF). After eliminating the constraint of the thin flame assumption, unsteady flamelet models have been successfully applied to supersonic combustion modelings [39–44]. Making the Taylor expansion of the nonlinear chemical source terms at the conditional mean, the influence of turbulence on chemistry can be closed on the first-order moments by neglecting the second- and higher-order correlations of Y'_α and T' [45]. The small fluctuation assumption is valid for most cases, except in the localized extinction/re-ignition regions [46], where the large fluctuations of the reactive scalars at a given mixture fraction value make the second-order conditional variances $\langle Y'_i Y'_i|\eta, x \in \text{zone}\rangle$ and conditional covariances $\langle Y'_i Y'_j|\eta, x \in \text{zone}\rangle$ nonnegligible. The higher-order moment closure approaches are extremely computationally expensive for large-scale chemical mechanisms because individual equations for all the species–species and species–temperature ($\langle Y'_i T'|\eta, x \in \text{zone}\rangle$) conditional covariances need to be solved, not to mention the complexity in constructing submodels for higher-order terms. As an alternative approach, conditioning on multiple variables, i.e., $Q_\alpha^{II} = \langle Y_\alpha|\eta = \xi(x,t), \theta = c(x,t), x \in \text{zone}\rangle$ with θ the sample space of additional variable c, can effectively reduce the fluctuations [47], and then the first-order closure of the conditional chemical source term remains valid. However, the transport of multiply conditional mean in the space coordinated by the multiple conditioning variables is apparently complex and computationally expensive as well. To resolve this issue, the zone conditional mean can be extended to be a partially unconditional mean as $Q_\alpha = \int \langle Y_\alpha|\eta = \xi(x,t), \theta = c(x,t), x \in \text{zone}\rangle P(\theta)\,\mathrm{d}\theta = \langle Y_\alpha|\eta = \xi(x,t), x \in \text{zone}\rangle$, whose fluctuation Y'_α depends on the variation range of c within the zone. Through proper refining and dynamically adjusting the zone, the variation of θ spans a small bin over the ensemble c space, and the partially unconditional mean Q_α takes advantage of having small Y'_α while avoiding the construction of multiply conditional equations. The zone can be divided explicitly according to multiple variables, zone $\equiv \{\eta \in [\xi - \varepsilon, \xi + \varepsilon], \theta \in [c - \varepsilon, c + \varepsilon]\}$, with ε a small quantity. By choosing suitable multiple conditioning variables for the zone division, the fluctuations around the partially conditioned mean can be reduced in comparison with the traditional singly conditioned mean.

The transport equations with differential diffusion for instantaneous mixture fraction ξ and mass fraction of individual species Y_α are

$$\frac{\partial \rho}{\partial t} + \nabla \cdot (\rho \boldsymbol{U}) = \dot{m}_p \tag{22}$$

$$\frac{\partial \rho\xi}{\partial t} + \nabla \cdot (\rho \boldsymbol{U}\xi) = \left(\rho \frac{\partial \xi}{\partial t} + \rho \boldsymbol{U} \cdot \nabla \xi\right) + \xi\left(\frac{\partial \rho}{\partial t} + \nabla \cdot (\rho \boldsymbol{U})\right) - \nabla \cdot (\rho D_\xi \nabla \xi) = \dot{m}_p \xi_l \tag{23}$$

$$\frac{\partial \rho Y_\alpha}{\partial t} + \nabla \cdot (\rho \boldsymbol{U} Y_\alpha) = \left(\rho \frac{\partial Y_\alpha}{\partial t} + \rho \boldsymbol{U} \cdot \nabla Y_\alpha\right) + Y_\alpha\left(\frac{\partial \rho}{\partial t} + \nabla \cdot (\rho \boldsymbol{U})\right) - \nabla \cdot (\rho D_\alpha \nabla Y_\alpha) = \dot{m}_p Y_{l,\alpha} + \rho W_\alpha \tag{24}$$

The mass fraction is a conserved scalar describing the mixedness of reactants having no chemical source term but may vary with the phase change. To include the differential diffusion effect, the definition of mixture fraction in the two-feed system can be based on the elemental mass fractions [48]. In flamelet models, the mixture fraction is only introduced as a means to parameterize the fuel-to-oxidizer mass ratio, and its relationship with the species is solved on the fly. ξ_l is the liquid composition expressed in mixture fraction, and it has $\xi_l = \sum Y_{l,\alpha}$, with $Y_{l,\alpha}$ the mass fraction of species α in the liquid phase. Differentiating Eq. (21), substituting it into Eq. (24), and then combining with Eqs. (22) and (23) yields

$$\rho \frac{\partial Q_\alpha}{\partial t} + \rho \boldsymbol{U} \cdot \nabla Q_\alpha + \mathrm{Y}_\alpha \dot{m}_p - \dot{m}_p Y_{l,\alpha} - \rho D_\alpha (\nabla \xi)^2 \frac{\partial^2 Q_\alpha}{\partial \eta^2} + \frac{\partial Q_\alpha}{\partial \eta}\underbrace{\left(\rho \frac{\partial \xi}{\partial t} + \rho \boldsymbol{U} \cdot \nabla \xi - \nabla \cdot (\rho D_\xi \nabla \xi)\right)}_{\dot{m}_p \xi_l - \dot{m}_p \xi} + \left(1 - \frac{D_\alpha}{D_\xi}\right) \nabla \cdot \left(\rho D_\xi \nabla \xi\right) \frac{\partial Q_\alpha}{\partial \eta} + \left(\rho \frac{\partial Q'_\alpha}{\partial t} + \rho \boldsymbol{U} \cdot \nabla Q'_\alpha - \nabla \cdot (\rho D_\alpha \nabla Q'_\alpha)\right) - \rho D_\alpha \nabla \xi \cdot \nabla \left(\frac{\partial Q_\alpha}{\partial \eta}\right) - \rho D_\alpha \nabla^2 Q_\alpha = \rho W_\alpha \tag{25}$$

Taking conditional average on Eq. (25) with the conditions 1) $\xi(x,t) = \eta$, and 2) sampling within the local zone $x \in$ zone, the representative flamelet equation for conditional species Q_α is

$$\rho_\eta \frac{\partial Q_\alpha}{\partial t} + \rho \langle \boldsymbol{U}|\eta\rangle_{\text{zone}} \cdot \nabla Q_\alpha + E_{\text{vap}} + E_{\text{ZFM}} = \rho_\eta \frac{D_\alpha}{D_\xi} \chi |\langle \eta \rangle_{\text{zone}} \frac{\partial^2 Q_\alpha}{\partial \eta^2} + \rho_\eta \left(\frac{D_\alpha}{D_\xi} - 1\right) M_\eta \frac{\partial Q_\alpha}{\partial \eta} + \rho_\eta \langle W_\alpha|\eta\rangle \tag{26}$$

With

$$E_{\text{vap}} = \langle \dot{m} \rangle_{\text{pzone}} \left(Q_\alpha - Y_{l,\alpha} + \frac{\partial Q_\alpha}{\partial \eta}(\xi_l - \eta)\right) \tag{27}$$

$$E_{\text{ZFM}} = \underbrace{\left\langle \rho \partial Q'_\alpha / \partial t + \rho \boldsymbol{U} \cdot \nabla Q'_\alpha - \nabla \cdot (\rho D_\alpha \nabla Q'_\alpha) \middle| \eta \right\rangle_{\text{zone}}}_{e_Y} - \left\langle \rho D \nabla \xi \cdot \nabla \left(\frac{\partial Q_\alpha}{\partial \eta}\right) \middle| \eta \right\rangle_{\text{zone}} - \langle \nabla \cdot (\rho D \nabla Q_\alpha)|\eta\rangle_{\text{zone}} \tag{28}$$

E_{vap} represents the contribution from the phase exchange, $\langle \dot{m} \rangle_{\text{pzone}}$ is the zone-averaged phase change rate, and for pure liquid droplets $\xi_l = 1$. Because of the inhomogeneous evaporation behaviors of droplets, the liquid fuel composition $Y_{l,\alpha}$ may vary from location to location. The implementation of two-phase DZFM requires that the liquid droplets approximately have the same composition within the zone. In the above equations, $\rho_\eta = \langle \rho|\eta\rangle$, and zonal conditional diffusion $M_\eta = \langle \nabla \cdot (D_\xi \nabla \xi)|\eta\rangle_{\text{zone}}$. The zone conditional mean of scalar dissipation rate $\langle \chi|\eta_{\text{zone}}\rangle$ is estimated by amplitude mapping closure (AMC) model [49] with the input of the mean scalar dissipation rate $\tilde{\chi}$ [50,51], which is calculated including both the resolved and subgrid contributions:

$$\tilde{\chi} = \underbrace{\mathrm{D}_\xi |\nabla \tilde{\xi}|^2}_{\text{resolved}} + \underbrace{\frac{\nu_{\text{sgs}}}{Sc_t} |\nabla \tilde{\xi}|^2}_{\text{subgrid}} = \underbrace{\mathrm{D}_\xi |\nabla \tilde{\xi}|^2}_{\text{resolved}} + \underbrace{\frac{\nu_{\text{sgs}}}{Sc_t} \frac{\tilde{\xi'^2}}{\mathrm{C}_{\text{var}} \Delta^2}}_{\text{subgrid}} \tag{29}$$

The local filter length Δ is replaced by the length scale d_{IDDES} of improved delayed detached eddy simulation (IDDES) in this study. The second term on the left-hand side in Eq. (26) represents the convection between flamelets with their neighbor zones and corresponds to the physical picture that the downstream flamelets can inherit the upstream flamelet status and continue the reactions, which is the key in reproducing the ignition process and the flame liftoff distance. The first and second terms on the right-hand side represent the diffusion in the mixture fraction space caused by scalar dissipation and differential diffusion. The last term on the right-hand side characterizes the effect of chemical reactions within each sampling bin of the mixture fraction space. For supersonic flows typically with a high Reynolds number of $Re \sim 10^5$–10^7, it has $\langle \rho D_\alpha \nabla \xi \cdot \nabla (\partial Q_\alpha / \partial \eta)|\eta\rangle_{\text{zone}} \sim \rho D_\alpha \xi D_\alpha^{-1/2} \cdot Q_\alpha \sim D_\alpha^{1/2} \sim Re^{-1/2} \approx 0$ and $\langle \nabla \cdot (\rho D \nabla Q_\alpha)|\eta\rangle_{\text{zone}} \sim \rho D \cdot Q_\alpha \sim Re^{-1} \approx 0$; accordingly, the second and third terms on the right-hand side in Eq. (28) can be neglected.

In supersonic flows, the density and velocity are primarily influenced by the compressibility (Mach number) while having a weaker correlation with mixture fraction. Instead of constructing separated models for $\langle \boldsymbol{U}|\eta\rangle$ and $\langle\rho|\eta\rangle$, the mass flux as a whole can be approximated by its mean value $\langle\rho\boldsymbol{U}|\eta\rangle = \rho\boldsymbol{U}$ assuming mass conservation across the mixture fraction space. In consideration of the weak correlation between density and mixture fraction in supersonic flows, the density fluctuation can be neglected as $\langle\rho|\eta\rangle = \rho$. Then it yields

$$\int \langle e_Y|\eta\rangle_{\text{zone}} P(\eta)\,\mathrm{d}\eta = \langle e_Y\rangle_{\text{zone}} = \rho\partial\langle Q'_\alpha\rangle_{\text{zone}}/\partial t + \rho\boldsymbol{U}\cdot\nabla\langle Q'_\alpha\rangle_{\text{zone}} - \nabla\cdot\langle\rho D\nabla Q'_\alpha\rangle_{\text{zone}} = 0 \tag{30}$$

Equation (30) indicates that the effect of e_Y is redistributing conditional variables in the mixture fraction space, and the ensemble redistribution effect is statistically conserved in the mixture fraction space. Through adaptively updating the zone division to make each zone corresponds to a narrow subspace of mixture fraction $\eta \in [\overline{\xi}_{\text{zone}} - \Delta\xi/2, \overline{\xi}_{\text{zone}} + \Delta\xi/2]$, where $\overline{\xi}_{\text{zone}}$ is the mean mixture fraction within the local zone, $\Delta\xi$ is the spanning bin width of fluctuations. Further refining the zone division to shrink $\Delta\xi$, the PDF in the zone collapses to a Dirac δ function centered at $\eta = \overline{\xi}_{\text{zone}}$. Then it has $\int\langle e_Y|\eta\rangle_{\text{zone}}\delta(\eta-\overline{\xi}_{\text{zone}})\,\mathrm{d}\eta = \langle e_Y|\eta=\overline{\xi}\rangle_{\text{zone}} = 0 \Rightarrow \langle e_Y|\eta=\xi\rangle_{\text{zone}} = 0$, implying that the conditional fluctuation transport in Eq. (28) can be neglected through dynamic zone adaption. In this study, no liquid evaporation exits; thus E_{vap} can be ignored. The final governing equation for conditional species in DZFM can be simplified as Eq. (7). By adapting the zone division, a local statistically homogeneity of conditional variables can be satisfied within each zone; i.e., there is no statistical dependence of the local states on space other than the conditioning variable ξ. Thus the spatial derivatives of Q_α in Eq. (7) can be taken to be zero within the zone ($\nabla Q_\alpha = 0$), and only the flux across zones needs to be taken into account.

The conditional temperature is obtained from the statistically averaged enthalpy and the conditional species as $Q_T = f(\langle H|\eta\rangle, Q_\alpha)$. The conditional temperature controls the progress of chemical reactions within each zone. The statistically averaged enthalpy is obtained by a historical statistics method, which computes a mass-weighted average of all of the filtered density function (FDF) in the CFD cells within the zone and across time steps over one flow-through time [52]:

$$\langle H|\eta\rangle = \frac{1}{n}\sum_{t_{i-n}}^{t_i}\frac{\int_{\text{zone}}\bar{\rho}\,\tilde{H}\,P(\eta)\,\mathrm{d}V}{\int_{\text{zone}}\bar{\rho}P(\eta)\,\mathrm{d}V} \tag{31}$$

where n is the sampling time steps, and $\overline{\rho}P(\eta)dV$ gives the filtered mass within one filter width around η. Such a statistical method is especially suitable for high-resolution LES and is apparently more computationally efficient than directly resolving a conditional energy equation. The compressibility effect can also be accounted for [40,43]. Similarly, $M_\eta = \langle\nabla\cdot(D_\xi\nabla\xi)|\eta\rangle_{\text{zone}}$ can also be obtained through conditionally filtering the mean values using the density weighted FDF:

$$M_\eta = \frac{1}{n}\sum_{t_{i-n}}^{t_i}\frac{\int_{\text{zone}}\nabla\cdot\langle(D_{\tilde{\xi}}\nabla\tilde{\xi})\cdot\overline{\rho}P(\eta)\,\mathrm{d}V}{\int_{\text{zone}}\overline{\rho}P(\eta)\,\mathrm{d}V} \tag{32}$$

The mean species mass fractions $\tilde{Y}_\alpha$ are then recovered by PDF weighted integration:

$$\tilde{Y}_\alpha = \int Q_\alpha(\eta)P(\eta)\,\mathrm{d}\eta \tag{33}$$

where $P(\eta)$ is the PDF describing the distribution of instantaneous ξ within the zone. Here, the β-function PDF is used because of its continuous shape for integration and the implication of δ-function in its expression. $P(\eta)$ is given as a function of the mean mixture fraction $\tilde{\xi}$ and its variance $\tilde{\xi''^2}$. The mean temperature can be reversely calculated from the mean enthalpy given the species composition $\tilde{T} = f(\tilde{H}, \tilde{Y}_\alpha)$.

The zone is divided according to different indices, as shown in Table 2. In the DZFM implementation, the domain is divided according to $\tilde{\xi}$, $\tilde{\xi''^2}$ (equivalent to scalar dissipation rate), Ma, as well as the streamwise distance x_i. For ZNM, Z-DAC, and Z-ISAT, p, T, and $\tilde{\xi}$ are used to ensure the local homogeneity of thermochemical states. For the nonequilibrium cases, T is calculated as Park's overall temperature T_p. To unify the zone division, the five indices of p, T, $\tilde{\xi}$, $\tilde{\xi''^2}$, Ma, and x_i are used for all the models. The streamwise distances are used to distinguish the flow residence time of the reacting mixture, and a total of 200 slices are cut in the whole streamwise direction. The division numbers in the ensemble space of $p, T, \tilde{\xi}, \tilde{\xi''^2}$, and Ma are 10, 50, 91, 20, and 10, respectively. For $\tilde{\xi}$, a denser distribution is clustered around the stoichiometric mixture fraction ξ_{st} to better resolve the flame front, e.g., 50, 30, and 20% of the grid points are laid in the space intervals $[0, \xi_{\text{st}}]$, $(\xi_{\text{st}}, 2\,\xi_{\text{st}}]$, and $(2\,\xi_{\text{st}}, 1]$, respectively. The sensitivity analysis for the zone division numbers has been conducted in the previous studies [36,53], and the current choice represents an optimization between fidelity and cost. The fidelity can also be confirmed by the flow consistency across the zones, i.e., no apparent aliasing for the mean variables. The zones divided by different indices intersect with each other, causing irregular and even discontinuous island-like regions. Those zones containing no CFD cells are deactivated in the current time step, with the corresponding zone flamelets temporally frozen. The total activated zone number varies with the flowfield and it is usually between 20,000 and 50,000 in this study. The zones are constantly updated to match each one with a narrow yet fixed subspace coordinated by the multiple zone division indices, in order of satisfy the DZFM premises, i.e., local homogeneity and small fluctuation.

F. OpenFOAM-Based Solver: Amber

The computation is conducted by a combined CFD package Amber, where the flow in three-dimensional spatial coordinate is solved by an OpenFOAM [54]-based solver AstroFoam, whereas the combustion and properties decoupled from the flowfield are solved by an in-house solver Multidimensional Burner (mBer). AstroFoam is designed for aeronautics and astronautics applications with the ability to model supersonic flow based on a low-Mach corrected hybrid KNP/central scheme [55–57], which can accurately resolve turbulence away from shocks while maintaining stability near the discontinuity. The combined solver Amber has been extensively validated for a wide range of combustor modelings [24,25,36, 58–62]. Through a flow-chemistry-property decoupling strategy, mBer is designed to treat the chemistry and property computation in the multidimensional thermochemical state-space coordinated by zone-averaged pressure, conditional temperature, and conditional species ($\overline{p} - Q_T - Q_\alpha$). The ingredient models in mBer, i.e., DZFM [33,35,36,63–65], ZNM [66], and ISAT and DAC [67], have been validated in previous studies. A shared-memory protocol for data exchange [68] has been developed to enable a convenient coupling of mBer with other closed-source flow solvers (e.g., FLUENT [69]). Such a shared-memory approach was not used in the current study as a direct code integration can be realized for the open-source flow solver AstroFoam [54].

Table 2 Unified zone division for DZFM, ZNM, Z-DAC, and Z-ISAT

Reaction type	Zone division indices
ZNM	$p, T, \tilde{\xi}$
Z-DAC	$p, T, \tilde{\xi}$
Z-ISAT	$p, T, \tilde{\xi}$
DZFM	$\tilde{\xi}, \tilde{\xi''^2}, Ma, x_i$

Figure 1 shows the coupling between the flow solver and the zone-based models. The flow equations and the zone-based models are solved in a segregated way at each time step, and no subiterations are required. The cell-based data obtained by the flow solver are averaged over each zone and passed to the zonal models, where the conditional means are PDF-weighted averaged over each CFD cell and fed back to the flow solver in the form of unconditional means. The flow solver solves the Navier–Stoker equations together with turbulence-related equations, i.e., IDDES based on Spalart–Allmaras (S-A) background RANS model [70] in this study. The zone-based conditional equations for species are solved with chemical source terms integrated by a CHEMKIN-II module [71]. The conditional temperature is obtained using a statistics method rather than directly resolved. Then the conditional relaxation time $\tau_{VT}|\eta$ is calculated based on the conditional species, conditional temperature, and zone-averaged pressure. Assuming a β-function PDF dependent of the mean mixture fraction $\tilde{\xi}$ and its variance $\tilde{\xi''^2}$, the mean species mass fraction, mean relaxation time can be directly calculated from the PDF integration of their conditional values. Already having the mean relaxation time, the energy equations for total enthalpy H and vibrational–electronic energy H_{vel} can be solved. The translational–rotational enthalpy H_{tr} is related as $H_{tr} = H - H_{vel}$. Then the mean temperatures, i.e., T, T_{tr}, and T_{vel}, can be iteratively computed given the mean enthalpies and the mixture composition.

The Z-DAC and Z-ISAT models are coupled with DZFM to speed up the solving of chemistry in the state space. Although the integration of chemical reactions has been significantly alleviated by clustering them from cell-based to zone-based, a large amount of chemical ordinary differential equation (ODE) systems roughly with the size of $50{,}000 \times 91$ (zone number multiplied by the discretization number in η space) are still required to be resolved. Because all the models share the same zone division topology, the total computational load is associated with the zone number. Once the zone division has been updated, the load is rebalanced among processors by allocating each processor with a similar number of zones. The information of chemical states can then be directly passed from the DZFM module to the Z-ISAT and Z-DAC modules for the assigned zones, without interprocessor communication anymore. The mechanism reduction in Z-DAC is conducted based on the representative chemical states of the current zone, which is given as the flamelet information in the η-bin corresponding to the zone-averaged mixture fraction. The coupling of Z-ISAT and Z-DAC can also be referred to as Z-TDAC [67]. The speed-up ratio of Z-TDAC increases with the increase of zone number and chemistry complexity. Under the current zone division, around 10% improvement in computational efficiency was achieved by Z-TDAC compared with the pure DZFM implementation, even with the additional data communication budget.

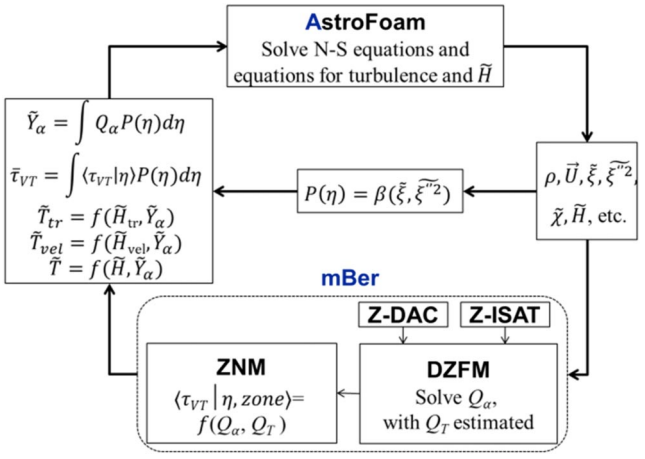

Fig. 1 Flow-chemistry-property coupling in Amber.

G. Experimental Case

In this study, the modeled REST scramjet has a desired flight Mach number of 12 and a dynamic pressure of $q = 50$ kPa, corresponding to an altitude of 36 km. The modeled geometry, including the planar forebody, as shown in Fig. 2, has an entire length of 1.435 m. The forebody has a length of 500 mm and is slightly wider than the inlet capture area. The 476.2-mm-long inlet section extends from the leading edge of the body to the throat. The lip of the inlet sidewall turns inward and closes completely, respectively, at 129.3 and 339.6 mm downstream of the inlet leading edge. The isolator section consists of two parts, i.e., the 29.67-mm-long former transiting from the inlet into an elliptic shape and the 25-mm-long latter with a constant-area elliptic shape. The total geometric compression ratio of the inlet is 6.61. The combustor section is connected to the isolator with a 1.25-mm-deep circumferential backward step. In the modeling, the combustor section is inclined with a 6° angle to redirect the flow toward the actual vehicle direction. The combustor section consists of a 161-mm-long constant-cross elliptical duct and a 121-mm-long diverging part at an expansion ratio of 1.6°. The nozzle section has a constant conic area expansion ratio of 5.

The inlet injection and combustion injection are combinedly used. The inlet injection is made of three 45°-inclined 2-mm-diam portholes on the backside of the compression surface at 755 mm downstream of the leading edge. The three inlet injectors are all located at the same streamwise plane with a spacing of 12.5 mm. Five 0.8-mm-diam injectors are positioned along the lower-half perimeter at the combustor entrance (1015.1 mm from the leading edge). Three of the five injectors are placed with one centered upon the centerline and the other two on either side with a spacing of 6.75 mm. The remaining two are placed horizontally on either side of the wall. The combustor injectors were inclined 45° to the local wall normal. The total fuel mass flow rate of 1.75002 g/s is split 29/71 between the inlet injection and the combustor injection to achieve a combined global equivalence ratio of $\Phi = 1.24$, which is calculated accounting for both O_2 and O. The test conditions of the air crossflow and the hydrogen stream are summarized in Table 3.

H. Numerical Configurations

The 1.435-m-long domain, including both the external and internal regions, is meshed with 92.52 million unstructured cells by using the Cartesian cut-cell immersed boundary (IB) method [72,73], which firstly generates a background Cartesian mesh and then cut the volume by the immersed boundaries into nonstaggered cells, e.g., tetrahedral, wedge, and pyramid cells. Because only those regions near the boundaries and corners are meshed by irregular-shaped cells, while most of the internal domain is meshed by

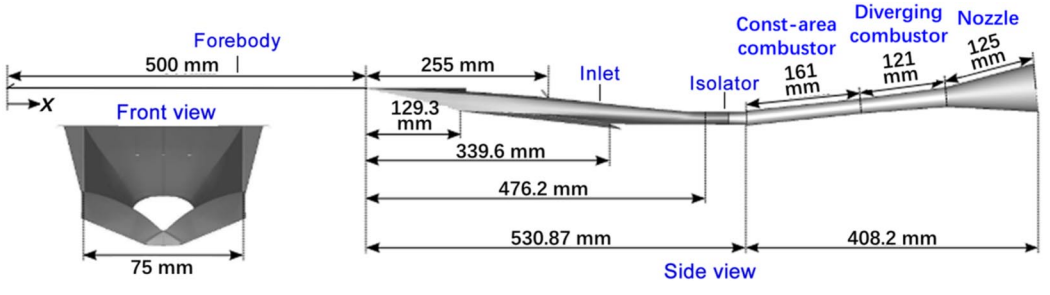

Fig. 2 Geometry and dimensions of the REST scramjet with planner forebody.

Table 3 Summary of test conditions and corresponding flight conditions

Quantity	Test condition	Flight condition
p, Pa	1176.6	398.66
U, m/s	3630.2	3678.41
T, K	386.79	243.71
ρ, kg/m^3	0.010507	0.00569
Ma	9.183	11.75
q, kPa	69.23	38.55
H_0, MJ/kg	7.01	7.01
Re	1.695×10^6	1.34×10^7
Y_{N_2}	0.72845	0.767
Y_{O_2}	0.18372	0.233
Y_{NO}	0.082728	0
Y_O	0.005102	0
$\dot{m}_{H_2,inlet}$, g/s	0.502635	— —
$\dot{m}_{H_2,combustor}$, g/s	1.246795	— —
T_{0,H_2}, K	298	— —
Ma_{H_2}	1.0	— —

hexahedrons, the overall mesh quality is usually excellently good, even for complex geometry with shape transition as in this study. The mesh is adaptively refined and clustered around the injectors by a growth ratio of 1.03. The maximum cell size is 0.8 mm, and the minimum size around the injectors is 75 μm. The boundary layer is meshed by 15 inflation layers with a total thickness of 1 mm, and the first near-wall layer of a dimensionless wall distance of $y^+<1$. High-quality uniform hexahedral grid cells are used for most of the domain, while tetrahedron, wedge, or pyramid cells filled only in large-curvature regions. Mesh quantity analysis shows that cells in 99.4% of the domain volume have skewness less than 0.5, and cells in 99% of the domain volume have orthogonal quality larger than 0.5. To verify the grid dependence, three additional mesh sets with 23, 40.48, and 59.38 million cells are generated by relaxing the limits of the maximum cell size.

The combustion chemistry is modeled by the 13-species and 33-step hydrogen combustion mechanisms developed for supersonic combustion modeling by Jachimowski [74]. To model the nonequilibrium chemistry of atmospheric air, a five-species mechanism [75–77] with three dissociation reactions for diatomic species and two exchange reactions involving NO is added to Jachimowski's mechanism. It is noted that the reactions in the nonequilibrium air chemistry have been duplicated in Jachimowski's combustion mechanism. However, their coefficients are calibrated for different purposes, i.e., one for combustion while the other for air dissociation. The original coefficients were all retained to model the different reacting behaviors of air. The reaction-rate coefficients for the nonequilibrium air chemistry are summarized in Table 4. The ionization of air species is only activated at a very high temperature, for example, in the postshock region of a crossflow over 10 km/s [7]. For the current study, with most of the temperature below 4000 K and a maximum velocity of 3.6 km/s, ionization can be safely ignored. The equilibrium constants to determine the backward reaction-rate coefficients are calculated as a polynomial function of temperature [78],

$$K_{eq} = \exp(A \cdot Z^5 + B \cdot Z^4 + C \cdot Z^3 + D \cdot Z^2 + E \cdot Z + F), \quad \text{with } Z = \ell_n(10^4/T) \tag{34}$$

The molecular viscosity is calculated by Blottner's viscosity model [79], and the thermal conductivity is given by Eucken's formula [80]. Specific heat and enthalpy are calculated by temperature-dependent curve-fit models [81]. The vibrational and electronic enthalpies are calculated based on their characteristic temperatures and the degeneracy degree of electronic level [2]. The mass diffusivities of individual species are calculated using the chemical kinetics package CHEMKIN-II [71] based on a CHEMKIN-format transport database. The mixture-averaged transport properties are calculated by the modified Wilke's mixing law [82,83]. The thermal and mass diffusion fluxes are given by Fourier's law [84] and modified Fick's law to ensure that the sum of the diffusion mass fluxes is zero [85].

Fixed pressure, temperature, velocity, and mixture compositions listed in Table 2 are specified on the inlets of the crossflow and the fuel jets. It is assumed that the incoming air is in vibrational equilibrium, and both the translational and vibrational temperatures are set to equal to the static temperature. A RANS-type turbulent inlet boundary condition is specified on the inlets, and a nominal turbulence viscosity is specified as $\nu_t/\nu = 1$. The walls were given a nonslip, isothermal boundary condition with a fixed wall temperature of 300 K because the experimental test time is short enough to prevent the viscous heating from taking effect. The open boundary condition is applied to the nozzle exit, where zero gradients are used for the outflow, and the environmental flow conditions are specified for the backflow.

The modelings were performed by the supersonic flow and combustion solver Amber. The convective fluxes are discretized using a low-dissipative hybrid scheme [55–57], combining the dissipative KNP scheme [86] with the nondissipative central scheme [87]. A third-order low-dissipation discretization scheme SSD [88] is applied for spatial discretization. The time step is advanced by the second-order Crank–Nicolson scheme [89].

MPI parallel computations based on domain decomposition were performed in TianHe-3E cluster composed of Phytium FT1500a CPU cores with a base frequency of 1.8 GHz. All the computations were conducted with 512 decomposed partitions assigned on 512 cores. The time step is limited both by a maximum Courant number of 0.5 and a user-specified maximum time step of 5×10^{-8} s, which is roughly 1/10–1/20 of the chemical time scale in intense combustion regions. The flush through time (FTT) is defined based on the length of the combustor flow-path length (1.435 m), and the initial flow speed of the vitiated air crossflow (3630.2 m/s) is 0.395 ms. The modeling case with 92.52 million cells takes $8 \times 24 \times 500$ CPU hours to ensure at least 4 FTTs for the data sampling and statistics.

Table 4 Nonequilibrium chemistry employed for atmosphere air

Reaction: $k_f = AT^\beta \exp(-T_a/T)$	A, cm^3/(mol · s)	β	T_a, K
Dissociation			
$O_2 + M = 2O + M$	2.000E + 21	−1.50	5.950E + 04
N_2/1.0/O_2/1.0/NO/1.0/N/5.0/O/5.0/			
$N_2 + M = 2N + M$	7.000E + 21	−1.60	1.1320E + 05
N_2/1.0/O_2/1.0/NO/1.0/N/4.286/O/4.286/			
$NO + M = N + O + M$	5.000E + 15	0.00	7.5500E + 04
N_2/1.0/O_2/1.0/NO/1.0/N/22.0/O/22.0/			
Exchange			
$N_2 + O = NO + N$	6.400E + 17	−1.00	3.840E + 04
$NO + O = N + O_2$	8.400E + 12	0.00	1.940E + 04

III. Results and Discussion

Figure 3a compares the predicted and measured static pressure on the body side for the equilibrium and nonequilibrium cases. The nonequilibrium combustion modeling needs to resolve additional equations for the trans-rotational energy and vibrational–electronic energy, as well as the relaxation between them, and the computational cost increases by around 40%. Grid independence is conducted based on the equilibrium combustion model for its relatively lower computational cost. Four mesh sets with 23 million cells, 40.48 million cells, 59.38 million cells, and 92.52 million cells are tested in this study. As the mesh is refined, the mean relative errors to the result of the finest mesh (92.52 million cells) are 3.5, 2.9, and 2.2%, which drop almost linearly with the characteristic grid size defined as the cubic root of the mean cell volume, as shown in Fig. 3b. The small error indicates that a grid convergence has been achieved, and the results of the finest mesh are used for the following analysis. The current LES predictions, whether based on equilibrium or nonequilibrium combustion models, agree well with the experimental data [9]. And the general trends are in accordance with the previous RANS modeling [9], which also incorporated the thermal nonequilibrium effect. The reflected shock wave impinging on the body side at $x = 0.96$ m causes a secondary pressure peak. Between $x = 1.1$ and 1.2 m, both the previous RANS prediction [9] and the current LES predictions reproduce a double-peak profile, where both are arisen by the reflections of compression wave due to flow redirection, and the heat addition strengthens the second. The current predictions match the measurement better in the latter part of the combustor and the nozzle. The sudden drop at $x = 1.3$ m is due to the geometry expansion. After incorporating the nonequilibrium effects, the peak drops slightly and agrees better with the experiment. In the inlet, isolator, and nozzle, the nonequilibrium prediction is lower than the equilibrium predictions.

Figure 4 compares the contours of key variables of the reacting internal flow assuming thermal equilibrium or nonequilibrium. As seen, significant differences exist between the two types of flowfields, emphasizing the importance of including the thermal nonequilibrium effects in the modeling of hypersonic combustion. The most notable difference is that the equilibrium temperature T is around 200 K higher than the trans-rotational temperature (Tt) in the combustor. Most of the flame temperature is higher than 2300 K in the equilibrium case, while only 2100 K in the nonequilibrium case. This is mainly because the energy transfer from trans-rotational energy to vibrational–electronic energy acts as a role of cooling. Then the weakened exothermic reactions further reduce the increase of Tt [90]. The flame stabilizes further downstream than in the equilibrium case, which has been reported in the previous DNS study [90]. The abrupt rise in vibrational–electronic temperature is slightly delayed than that of trans-rotational temperature because the thermal relaxation takes some time. The addition or deduction of kinetic energy is only from the trans-rotational energy; thus, the flow expansion in the nozzle causes a noticeable decrease of Tt, but no immediate influence on Tv. Tv needs some relaxation time to reach equilibrium with Tt again, but apparently, the nozzle is not long enough to contain the whole relaxation process. The energy transfer between trans-rotational energy and vibrational–electronic energy is negligible for $Tt < 800$ K, and therefore the rise in Tv is insignificant before the inlet. The near equivalence of Tt and T in the equilibrium case suggests that the air capturing of the inlet should be less influenced. In the inlet and isolator, the increase in stagnation enthalpy in the boundary layer activates the vibrational–electronic energy mode, whose cooling effect moderates the thickness of the enthalpy layer. With a thinner boundary layer, the locally increased dynamic pressure around the jet leads to a lower jet-to-crossflow momentum flux ratio and consequently a lower jet penetration depth. For this, the threadlike high-temperature region before the combustor injection is slightly thicker in the equilibrium case. From the comparison of Mach contours, the cooling effect has shown an observable alleviation in thermal choking. The shock impingement causes several boundary detachments. All those subsonic near-wall regions shrink under nonequilibrium. Because of the nonequilibrium cooling effect, the subsonic region in the upper mixing layer of the combustor caused by the heat addition shrinks as well and moves slightly downstream.

Chemical explosives mode analysis (CEMA) originated from computational singular perturbation (CSP) algorithm [91] was conducted to distinguish the chemical explosive mode and dissipative (relaxation) mode. Eigendecomposition of the chemical source term Jacobian yields the chemical modes. The reciprocal of the eigenvalue λ_i represents the time scale of the ith mode and was used to distinguish multiscale (fast/slow) dynamics. CEMA can be considered as a special version of CSP that focuses on the fastest mode, which corresponds to the eigenvalue λ_e with the largest magnitude. Following [92], negative λ_e corresponds to the relaxation mode, where chain termination reactions dominate and consume existing intermediate species; positive λ_e defines the explosive mode, where the chain branching steps must be overall exothermic and overbalances the chain termination steps. Both the relaxation mode and explosive mode drive the reacting system toward chemical equilibrium (with $\lambda_e = 0$). Figures 4f and 4g show the signed log-scaling of the CEMA variable, $\text{sign}(\lambda_e) \times \log_{10}(1 + |\lambda_e|)$, where a minimum of 1 s^{-1} is added to filter out the chemically inactive zone denoted by $|\lambda_e| < 1$. From the current modeling, no explosive region ($\lambda_e > 1$) of significant size has been identified in the reacting field. The explosive mode usually occurs in the transient ignition process. However, judging from the trajectory of the fuel stream, the ignition regions in hypersonic flow have been highly stretched by the crossflow to be thin yet long, thus significantly relaxing the reaction progress and explosiveness. The wide distribution of negative λ_e denotes that postignition and diffusion-controlled chemistry occurs in most of the flowfield. Intense oxidation reactions and also chain termination steps dominate in the reacting shear/mixing layer as denoted by $\lambda_e < -10^7$ s^{-1}. After incorporating the nonequilibrium air chemistry, air dissociates under high temperature even without the fuel, as in the threadlike regions with $\lambda_e < -10^7$ s^{-1} before the combustor injection. Those additional air dissociation regions act as the role of radical farming [93], which

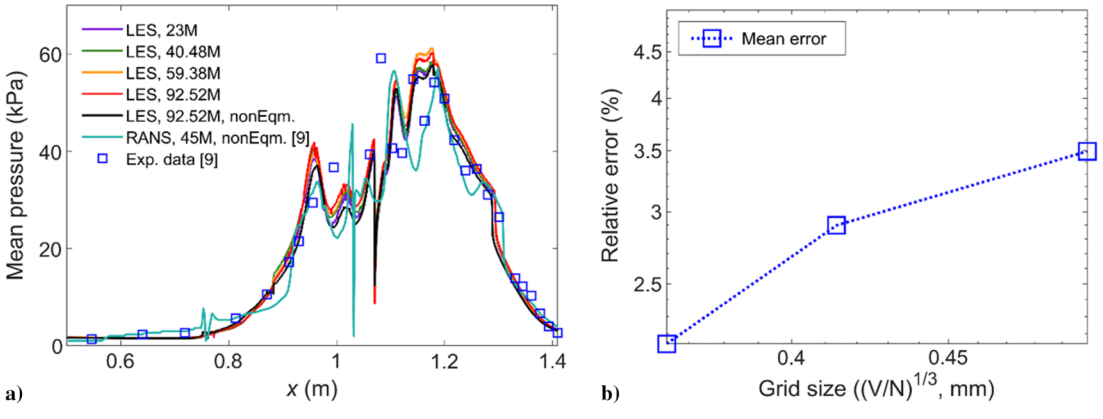

Fig. 3 a) Streamwise mean static pressure on the body side; b) grid convergence behavior.

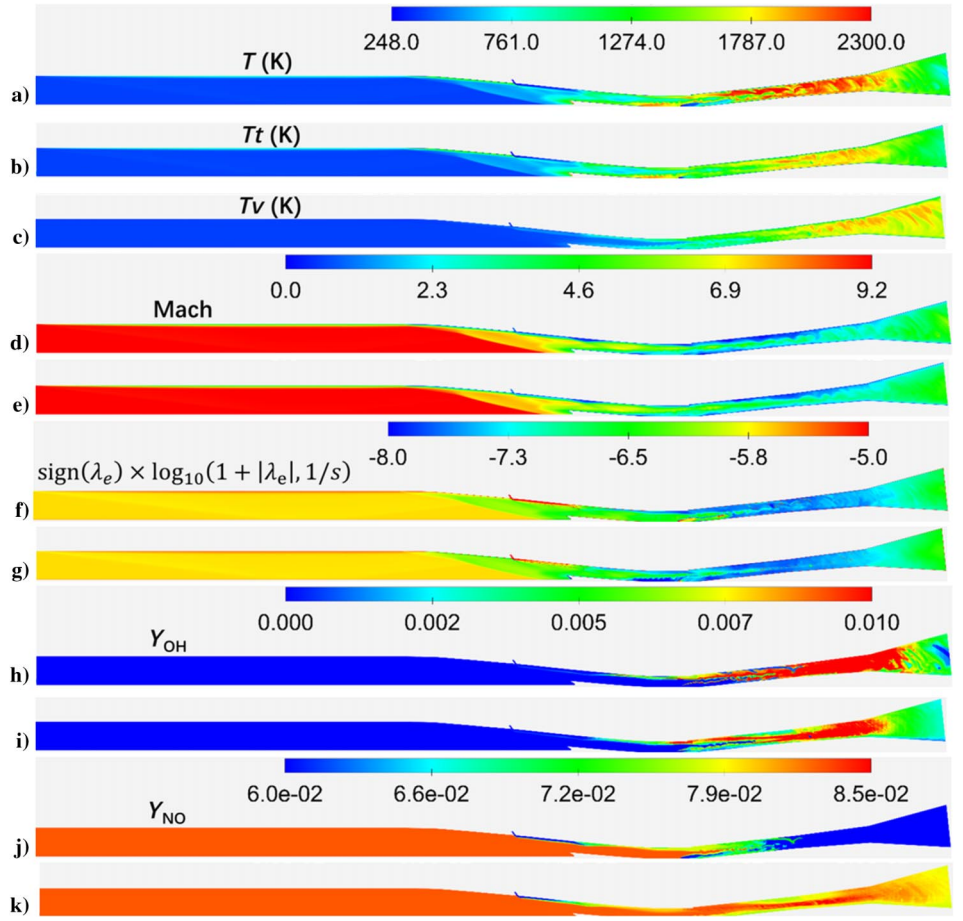

Fig. 4 Contour of a) T in the thermal equilibrium case, and contours of b) Tt and c) Tv in the nonequilibrium case. Contours of d) Mach number, f) signed log-scaling of CEMA, h) OH mass fraction, and j) NO mass fraction in the nonequilibrium case. Contours of e) Mach number, g) signed log-scaling of CEM eigenvalue λ_e, i) OH mass fraction, and k) NO mass fraction in the equilibrium case.

intensifies the downstream reactions as evidenced by the larger λ_e magnitude. Even with the help of radical farming, the leaner OH suggests an overall degenerated reactivity due to the nonequilibrium cooling effect. According to the Tv contours, the cooling effect becomes prominent only after the diverging part of the combustor, before which the wider OH distribution highlights the positive effect of the radical farming in initiating hydrogen oxidation. In both cases, the inlet-injected hydrogen initiates chain reactions near the inlet cowl, but a stable ignition was not achieved until reaching the downstream injectors, whose flame then merges gradually with the upper one to form a bifurcated flame. NO is mostly consumed before the latter part of the combustor in the equilibrium combustion, whereas a large amount remains in the nonequilibrium case.

Both the heat addition due to combustion and the kinetic energy transfer due to flow compression/expansion can disturb the thermal equilibrium. From Fig. 5, the V-T relaxation time between the vibrational and translational energy modes (denoted by τ_{VT}) is 4.2 ms for the low-pressure and low-temperature external flow, where the excitation of vibrational mode has not been activated due to the low collision frequency and collision energy among molecules. Behind the precompression shock surface of the inward turning inlet, Tt increases, and the flow becomes thermal nonequilibrium. The V-T relaxation time decreases from 1 to 0.1 ms in the inlet and isolator sections. Given the large relaxation time, the flow maintains nonequilibrium when entering the combustor, where a complex coupling between the nonequilibrium effect and turbulent combustion needs to be addressed in the modeling. With the heat addition from the combustion, Tt increases more drastically over Tv, aggravating the nonequilibrium, but, on the other hand, reduces the cross-sectional averaged V-T relaxation time to be less than 0.1 ms inside the combustor. In the reacting shear/mixing layer with a high $Tt > 1600$ K, the V-T relaxation time decreases to a much lower

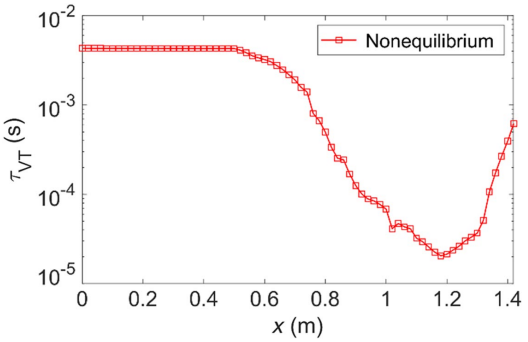

Fig. 5 Streamwise variation of V-T relaxation time in the nonequilibrium case.

value of the order of 10^{-5} s, which implies that a local thermal equilibrium status can be established. As observed from Figs. 4b and 4c, the difference between Tt and Tv gradually vanishes toward the diverging part of the combustor, which indicates that a short period of thermal equilibrium has been established there. Nevertheless, when entering the nozzle, Tt decreases due to the kinetic energy transfer and deviates from Tv once again. With the decreasing Tt, the relaxation time increases from 0.05 to 0.8 ms, which means that the nonequilibrium status was frozen until the outlet, considering the extremely short flow residence time in the nozzle. The production rate of vibrationally excited molecules and atoms from diatomic air molecules (i.e., N_2 and O_2) is proportional to the number density. The recombination reaction requires the presence of a third collision partner and is therefore proportional to the square of density [94]. The recombination of dissociated molecules nearly stops during the nozzle expansion as the density drops significantly [95]. Thus the

nozzle gas will remain dissociated when being injected into the freestream.

Figure 6 shows the quasi-one-dimensional performance analyses along the streamwise direction. The final mixing efficiencies are 90 and 96% for the equilibrium and nonequilibrium cases, respectively. The mixing efficiency is higher after the inlet injection, and a difference of around 6% was reached after the combustor injection. In the direct numerical simulation (DNS) study of supersonic jet flame [5], the presence of nonequilibrium was also observed to shorten the jet breakdown distance. It was concluded that the lower Tt reduces viscosity and leads to improved mixing through alleviating the lamination of the reacting shear/mixing layer [5].

Though with higher mixing efficiency, the final combustion efficiency in the nonequilibrium case is 66%, which is lower than the 80% in the equilibrium case. The fact that Tt is lower than T in the equilibrium case should be mainly responsible for the weaker reactivity. Another factor contributing to the reduced combustion efficiency is that the incorporation of nonequilibrium air chemistry produces radicals that are not fully recombined in the flow path. For example, there remains rich NO in the diverging part of the combustor in Fig. 4k. Those radicals containing H and O further deplete the available hydrogen or oxygen that can be converted to the final product H_2O. The weaker reactivity further leads to delayed flame stabilization [5]. From Fig. 6b, the inlet-injected fuel was ignited early in the equilibrium case to form an abrupt rise in the combustion efficiency, which is in accordance with the richer OH concentration before the isolator in Fig. 4h. Because of the radical farming, the nonequilibrium case gains a deflagration immediately after the combustor injection, but the reactivity then recedes with the increase of Tv. The previous RANS modeling [9] with vibrational nonequilibrium effects turned on predicted a final combustion efficiency of 84.87% and a final mixing efficiency of 98.87%. Because the perfectly stirred reactor combustion model was used in the previous RANS modeling [9], thus the value of 84% could be overpredicted. However, both the current LES modeling and the previous RANS modeling predict combustion efficiencies of over 80%, which is the minimum requirement to achieve thrust for access-to-space applications [96].

The total pressure in Fig. 6c is calculated accounting for the temperature-dependent variation of specific heat:

$$P_t = p \cdot e^{\int_T^{T_t} \frac{Cp(T)}{RT} \mathrm{d}T} \tag{35}$$

Under high stagnation temperature, the ideal isentropic relationship to determine P_t giving p, Ma, and assumed specific heat ratio γ is not valid anymore because the gas specific heat may vary significantly with temperature. The streamwise profiles of P_t loss coefficient are much similar for both cases, with the final total pressure loss of 98.5 and 99%, respectively. The only discrepancy between $x = 0.86$ and 1.14 m can only be attributed to the Rayleigh heating caused by the early ignition. The cooling effect of the rise in Tv in the boundary layer noticeably delayed the ignition of the inlet-injected fuel. The fact that Tv is of the same level as Tt in the diverging combustor indicates that the nonequilibrium cooling effect has become more significant. The higher reactivity in the equilibrium case causes a marginal increase in the total pressure loss.

The streamwise impulse force function in Fig. 6d is defined as the summation of pressure force and streamwise momentum flux $I = (p + \rho u_x^2)S$. The difference in streamwise impulse gives the streamwise force $F_{\mathrm{bx}} = \Delta I$ according to the conservation of momentum. The domain includes both the external and internal flow, where the moment is not conserved for the external flow because part of the flow has slipped away from the open boundaries. After the inlet injection, the nonequilibrium cooling effect suppresses the thickening of the boundary layer, which is equivalent to enlargement of the flow-through area; therefore, the streamwise impulse has a small rise before the isolator. Most of the thrust is produced in the mildly diverging combustor and the wide-angle diverging nozzle. Higher thrust is produced in the equilibrium case at the nozzle exit as more heat of combustion has been released to energize the engine.

As listed in Table 5, negative specific impulses of −611 and −365 s are produced under the equilibrium and nonequilibrium conditions, respectively. The mass capture rate is less influenced by the equilibrium simplification, and the current value of 58 g/s is close to the previous RANS prediction of 59.82 g/s [9]. The fuel supplying rate is automatically maintained at a unity equivalence ratio. After being precompressed by the inlet bow shock wave, the pressure at the isolator is raised to around 13 kPa for both cases. The ratio of peak pressure to the isolator pressure has an 8.7% drop from 2.9 to 2.7 when the nonequilibrium effect has been taken into

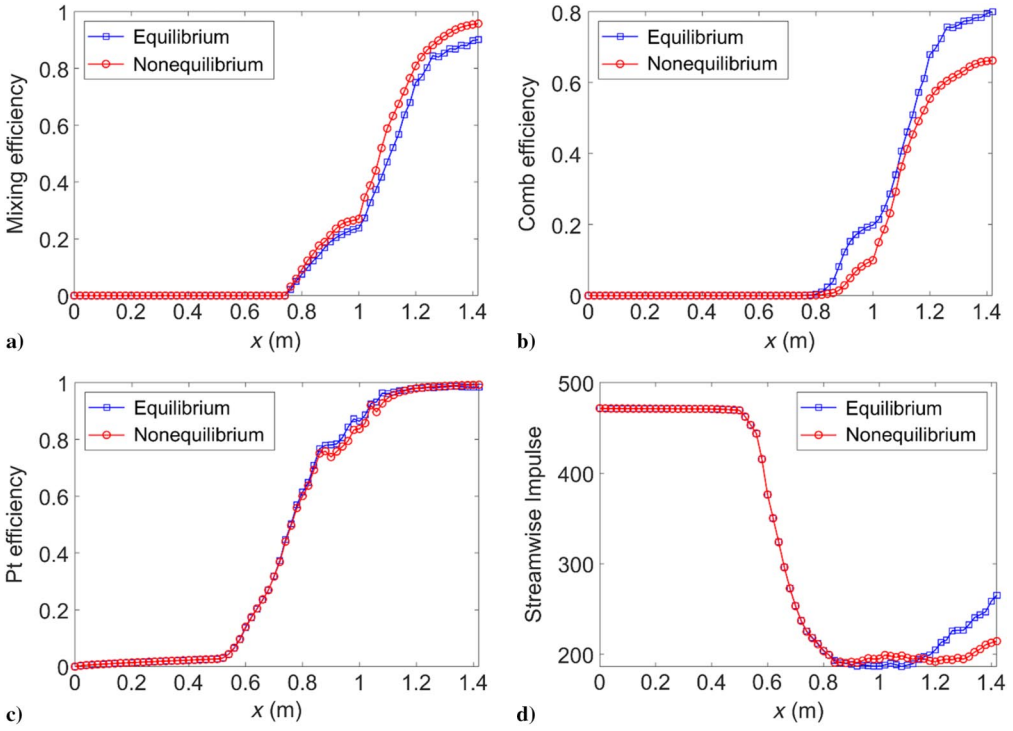

Fig. 6 Quasi-one-dimensional performance indices along the flow path: a) mixing efficiency, b) combustion efficiency, c) total pressure loss coefficient, and d) streamwise impulse force.

Table 5 Overall engine performance under equilibrium and nonequilibrium conditions

Global performance	Equilibrium	Nonequilibrium
Air captured rate, kg/s	0.057568	0.057904
Fuel flow rate, kg/s	0.0017494	0.0017494
Inviscid thrust, N	24.5919	20.0092
Viscous drag, N	−35.0812	−26.2696
Net thrust, N	−10.4893	−6.2603
Combustion efficiency	0.79942	0.66219
Isolator pressure, kPa	13.1298	12.9083
Peak pressure ratio	2.9372	2.6825
Specific impulse, s	−611.1962	−364.7819

account. Because of the weaker pressure rise, the inviscid thrust, i.e., the thrust produced by surface pressure on the engine walls, decreases from 25 to 20 N with the presence of nonequilibrium. The viscous drag due to friction decreases from 35 to 26 N under the nonequilibrium condition because the molecular viscosity decreases with the reduction of the flame temperature. A negative net thrust of −14.438 N was also reproduced in the previous RANS prediction [9], where the inviscid thrust is 17.805 N and viscous drag is −32.243 N. The previously predicted inviscid thrust of 17.805 N is comparable with the current nonequilibrium prediction of 20 N because both of them underpredict the pressure compared with the equilibrium prediction. The previously predicted frictional drag agrees better with the equilibrium prediction, probably because their combustion efficiency was closer.

Figure 7 shows the relative energy for the first 20 proper orthogonal decomposition (POD) modes for the temperature fields [97]. As seen, the first mode is dominant over the others, especially for the equilibrium case, where the first mode energy takes nearly one-third of the whole and doubles that of the nonequilibrium case. This shows that there exist large-scale unsteady and more energetic coherent structures in the equilibrium case. The mode energy decreases more gently with a reducing difference from the second mode, indicating a stochastic flame behavior. Figure 8 shows the first 4 POD modes for the two cases. The first POD mode for the equilibrium case shows the main reaction regions, which fill the combustor and extend into the nozzle to continue the residual reactions, causing a persistent rise in combustion efficiency. The second POD mode of the equilibrium case indicates those high-temperature spots, including the reacting shear/mixing layer in the inlet-injected fuel jet wake and the discontinuous "streaks" in the diverging combustor where the two jets merge. The high-temperature region before the combustor injection is not due to combustion but caused by the reflected shock wave. Figures 8c and 8d show the stochastic movement of the flame streaks, where intense combustion reactions controlled by the mixing take

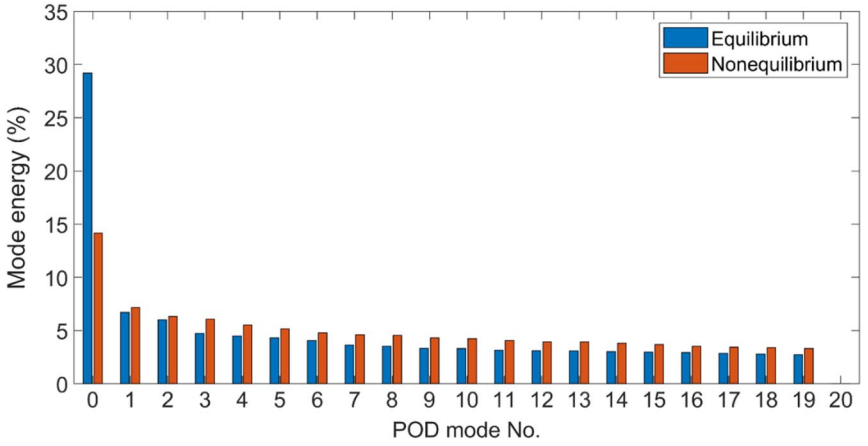

Fig. 7 Relative mode energy of the first 20 POD modes.

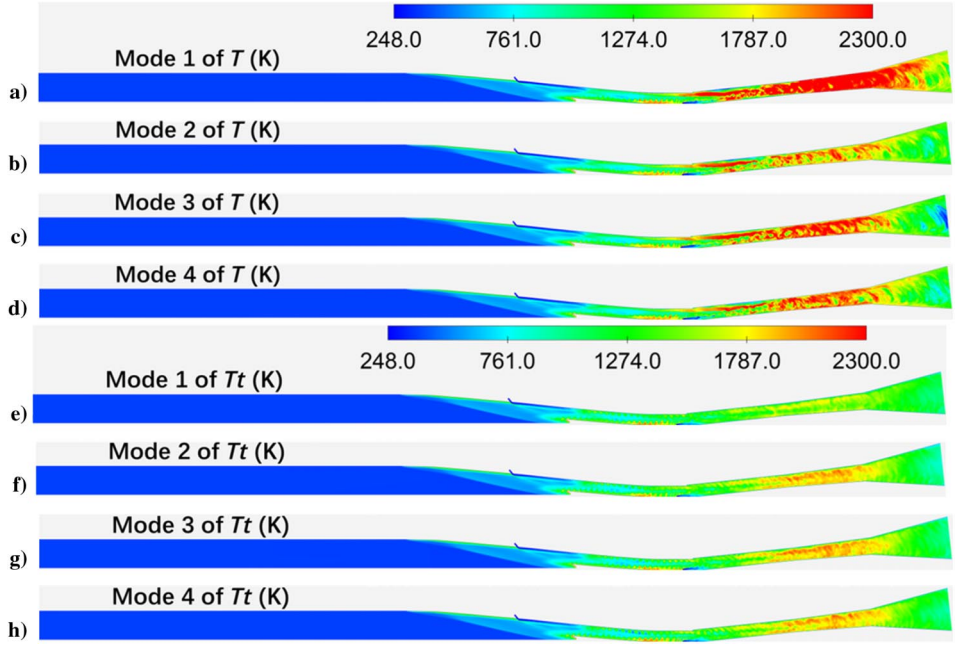

Fig. 8 The first four POD modes in the a–d) equilibrium and e–h) nonequilibrium cases.

place intermittently. The first POD mode in the nonequilibrium case shows that steady reactions occur in the wake of the two fuel streams, which attach to the upper and lower walls, respectively. Those weak steady reactions correspond to the initial chain reactions under fuel-rich conditions. The subsequent three POD modes are visually similar because the combustion is nearly premixed and more homogeneous due to the increase of the effective Reynolds number under the nonequilibrium condition. Although having sufficient mixing, the nonequilibrium cooling effect substantially reduces the flame temperature and quenches the flame in the nozzle, whereas the burning persists there for the equilibrium case.

Figure 9 counts the activation ratio of the reactions and the mechanism size in each zone during the Z-DAC reduction. The nonequilibrium air chemistry ($O_2/N_2/NO$ dissociation reactions and NO exchange reactions listed in Table 3) is only included in the nonequilibrium modeling and was retained in most zones with activation ratios larger than 98.6%. As seen, the first 13 reactions related to the oxidation of hydrogen are almost entirely retained. The reactions involving H_2O_2 (numbers 14–20) are only activated in regions with rich H/O/OH/HNO radicals, with activation ratios of around 77% in the equilibrium cases. The activation ratio of H_2O_2-related reactions is higher (93%) in the nonequilibrium cases, probably because H/O/OH/HNO radicals are abundantly produced when including air dissociation and cannot be completely consumed under lower flame temperature. The HNO- and NO_2-related reactions become important only at a temperature higher than 1800 K [98], which can be easily satisfied in high-Mach combustors; therefore, they were highly activated. Historical statistics in Fig. 9b show that 1) for the nonequilibrium case, 92.8% of the zones retain the complete mechanism with 38 reactions and 5.7% have a reduced mechanism with 31 reactions, and 2) for the equilibrium case, 74.5% of the zones retain the complete 33 reactions, and 20.2 and 2.4% of the zones adopt 26- and 29-step reduce mechanisms, respectively. Because of the good mixing and the radical farming effect, the nonequilibrium case has more probability of retaining the complete mechanism. Small subsets of the full mechanisms are more frequently used in the equilibrium case, suggesting more heterogeneous combustion, as also evidenced by the flame streaks in the POD modes.

Figure 10 shows the variations of major species extracted from the zone flamelets along the line connecting the combustor injector and the nozzle exit, i.e., $x = 1.03$, 1.13, 1.23, 1.33, and 1.43 m. The variations show the evolution of flamelets from a mixing status to nearly complete burning status. Figure 10a is probed in the jet wake, where the pure mixing was complete while the reactions were just started. Because of the radial farming [93] of O atoms from the upstream air dissociation, the initial chain reactions occur more quickly in the nonequilibrium case and produce more H_2O. Soon afterward, the more intense combustion in the equilibrium case consumes all the available oxygen and produces more H_2O than the nonequilibrium case, as shown in Fig. 10b. In Fig. 10c, the continue reactions deplete the oxygen atoms from NO and convert them to the final products H_2O, which is the reason why little NO is left in the latter part of the combustor in the equilibrium case while much more NO remains in the nonequilibrium case in Figs. 4i–4k. Following the physical picture of Eq. (7), the mixing proceeds along with the reactions. With the entrainment of fresh air, the residual hydrogen was consumed by the replenished oxygen as in Fig. 10d, and NO is regenerated under the conditions of high temperature (>1800 K) and abundant oxygen in the equilibrium case, but still in lower concentration than the nonequilibrium case. The reacting status in Fig. 10e is similar to Fig. 10d except with more replenished oxygen, indicating a nearly frozen chemistry in the nozzle, where the temperature drops due to the flow expansion. Although the air dissociation and NO exchange reactions are also included in the original hydrogen/oxygen combustion mechanism, the changes in reaction coefficients do influence the reaction path and induce different reacting behaviors.

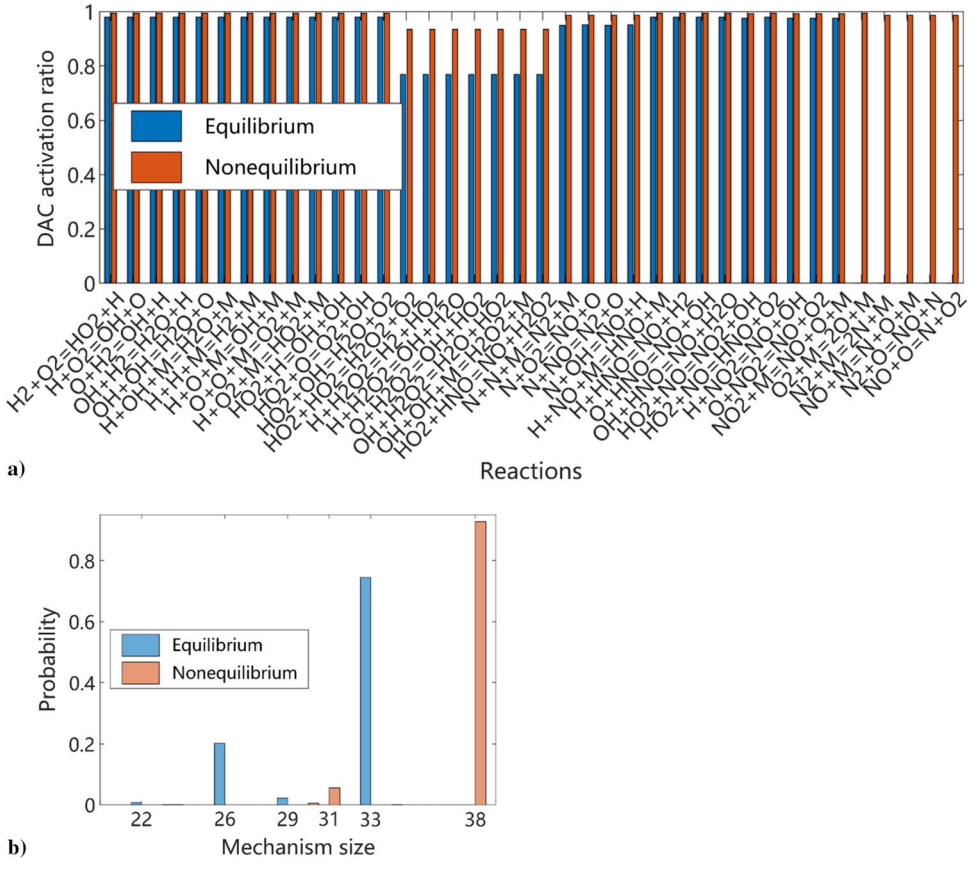

Fig. 9 a) Activation ratio of reactions and b) statistics of mechanism size in DAC.

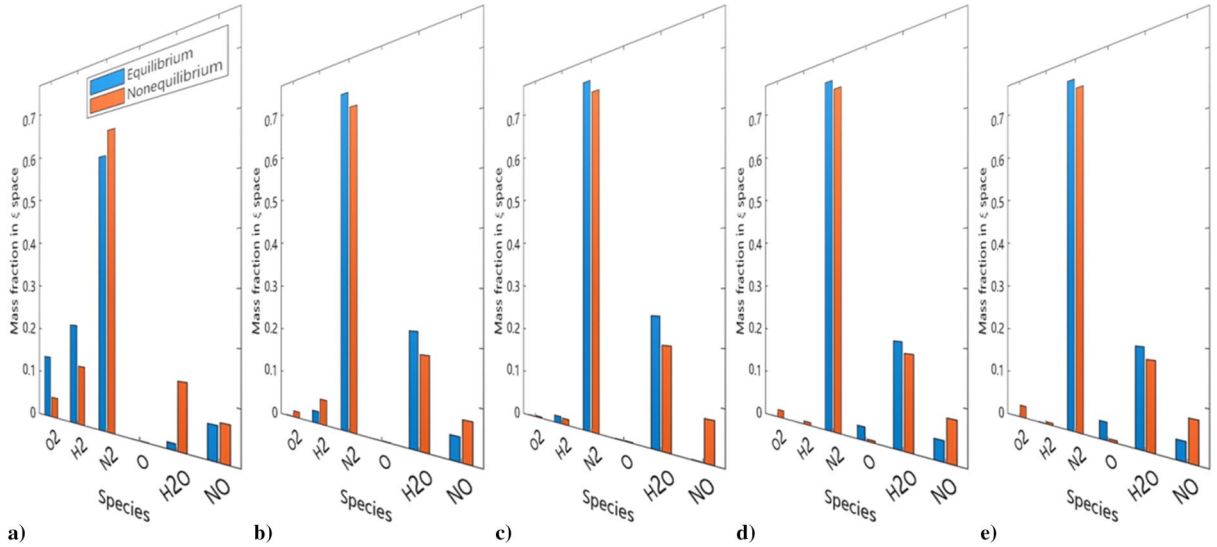

Fig. 10 Variation of major species from the combustor to the nozzle.

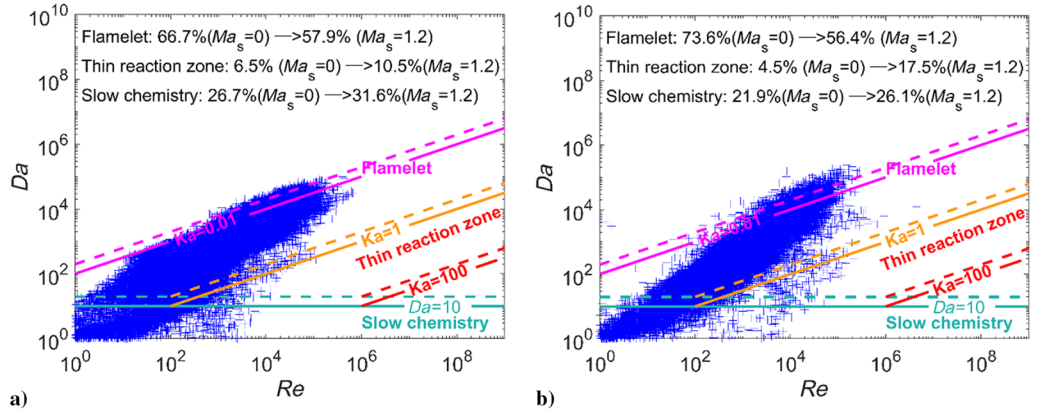

Fig. 11 Borghi diagram of turbulence–chemistry interaction modes in the DZFM zones: a) equilibrium case, and b) nonequilibrium case.

Figure 11 statistically analyzes the turbulence–chemistry interaction (TCI) modes in the DZFM zones based on Borghi diagram [99]. The Damköhler number (Da) is defined as the ratio of the turbulence time scale τ_t and characteristic time of chemical reactions τ_c, i.e., $Da = \tau_t/\tau_c$. When calculating the turbulence time scale based on LES data, it is necessary to include the resolved part of the turbulent fluctuation k_{res} [100], i.e., $\tau_t = (k_{\text{res}} + k_{\text{sgs}})/\epsilon$, where k_{sgs} is the SGS kinetic energy and ϵ is the turbulence dissipation rate. The characteristic time of chemical reactions τ_c is calculated as the reciprocal of the CEMA index. The Karlovitz number Ka is defined as the ratio of the characteristic time of chemical reactions to the smallest turbulence time scale (Kolmogorov time scale), i.e., $Ka = \tau_c/\tau_k$, where the Kolmogorov characteristic time is given by $\tau_k = (\nu/\epsilon)^{1/2}$, with ν the kinetic energy. Accordingly, there is the relationship for the Reynolds number, $Re(\tau_t/\tau_k)^2 = Da^2 \cdot Ka^2$. According to Ka and Da, the TCI relationships can be divided into three modes [99,101], i) flamelet mode with $Ka < 1$ and $Da > 10$, ii) thin reaction zone mode with $1 < Ka < 100$ and $Da > 10$, and iii) slow chemistry mode with $Ka > 100$ and $Da < 10$. The boundaries for those TCI modes are marked as the bold lines in Fig. 11. Under high Mach number, the flame speed is increased by a factor of $\sqrt{1 + Ma_s^2}$ due to the compressibility enhanced reaction rate [101]; thus the bold lines in Fig. 11 translate upward. Assuming a typical fluctuation of around 10% in supersonic combustion [101,102], the subgrid Mach number Ma_s is taken to be 1.2, and the corresponding boundaries are marked as the dashed lines. Under weak compressibility assumption, more than 2/3 of the zones are in the flamelet mode assuming fast chemistry, 4–7% of the zones are in the thin reaction zone mode, and less than 27% of the zones are in the slow chemistry mode. The compressibility effect drives the mode toward the regimes of thin reaction zone and slow chemistry, where the finite-rate effect becomes dominant over mixing. Despite the compressibility effect, the large portion of the flamelet mode of nearly 2/3 indicates that even for the hypersonic combustor with an extremely high incoming Mach number, the hydrogen reaction rate is still mostly faster than the local mixing time scale. For hydrocarbon-fueled supersonic combustion, the flamelet mode would usually decrease significantly to be less than 20% [103]. The high stagnation temperature downstream of the inlet further facilitates the air dissociation and hydrogen oxidation. Although with lower overall flame temperature, the flamelet mode distributes wider in the nonequilibrium case, probably owing to the good mixing. Moreover, as indicated by the larger magnitude of the CEMA variable for the nonequilibrium case, the radical farming effect of the air dissociation speeds up the reactions and drives the turbulent combustion toward the flamelet mode. The nonnegligible portion of slow chemistry implies that there is a wide range of turbulence–chemistry interactions that cannot be treated by the generic flamelet model, which treats the whole domain as a global zone [38]. The Reynolds number in the hypersonic combustor is as high as 10^6, so the Kolmogorov length scale is in the order of microns, which means that the DNS cost of hypersonic combustion is still currently unaffordable.

IV. Conclusions

This study proposed a ZNM based on the concept of zonal representation of the nonequilibrium relaxation times. ZNM, together with DZFM, Z-DAC, and Z-ISAT, forms the complete framework for nonequilibrium combustion modeling. Based on the concept of zonal conditional mean, a four-dimensional transport equation in the spatial and moment space is constructed. By satisfying the local homogeneity and small fluctuation assumptions, the equation can be closed with no spatially dependent terms within the zone as well as the first-order chemical source closure. Moreover, if the two-phase effect is coupled, a local homogeneity assumption of the droplet composition is required. All the above three assumptions can be satisfied through dynamically adapting and refining the zones based on multiple division indices. The framework is then applied to the IDDES modeling of a full-scale scramjet operating at Mach 12 with a total of 95.52 million cells.

Both the heat addition due to combustion and the kinetic energy transfer due to flow compression/expansion can disturb the thermal equilibrium. The V-T relaxation time becomes less than 0.1 ms inside the combustor, where a short period of thermal equilibrium status was established. Given the large relaxation time of more than 1 ms and the extremely short flow residence time, the gas remains nonequilibrium and dissociated in the rest domain.

The nonequilibrium has two effects on the flow, i.e., the cooling effect caused by the energy transfer from trans-rotational energy to vibrational–electronic energy and the radical farming effect added by the air dissociation. The cooling effect caused an overall lower Tt and can alleviate the thermal choking. After incorporating the nonequilibrium air chemistry, CEMA indicates that air dissociates under high temperature even without the fuel before the combustor injection. Those additional air dissociation regions intensify the downstream reactions through radical farming. Even with the help of radical farming, the overall reactivity still degenerates due to the cooling effect, as indicated by the leaner OH.

The nonequilibrium cooling effect increases the mixing efficiency from 90 to 96% by reducing the fluid viscosity but also brings down the combustion efficiency from 80 to 66%. POD analysis indicates that large-scale unsteady and more energetic coherent structures exist in the equilibrium case, whereas more homogeneous combustion in the nonequilibrium case due to the good mixing. Quasi-one-dimensional thrust analysis shows that higher thrust is produced in the equilibrium case as more heat was released, whereas the inlet mass capture behavior is less influenced. Negative specific impulses were produced for both cases.

Because of the good mixing and the radical farming effect, the nonequilibrium case has more probability of retaining the complete mechanism. Small subsets of the full mechanisms are more frequently used in the equilibrium case, suggesting more heterogeneous combustion. The compressibility effect drives the TCI mode toward the regimes of thin reaction zone and slow chemistry. Despite the compressibility effect, the large portion of the flamelet mode of nearly 2/3 indicates that even for the hypersonic combustor with an extremely high incoming Mach number, the hydrogen reaction rate is still mostly faster than the local mixing time scale. Although with lower overall flame temperature, the flamelet mode spans wider in the nonequilibrium case, owing to the good mixing and the radical farming.

Acknowledgments

The research was supported by National Key Research and Development Program of China (2019YFB1704202), the Strategic Priority Research Program of Chinese Academy of Sciences (Grant No. XDA17030X00), and Training Program of the Major Research Plan of the National Natural Science Foundation of China (Grant No. 91641110). The authors are also grateful to the National Supercomputer Center in Tianjin for providing the computational resource.

References

[1] Anderson, J. D., "Chemical and Vibrational Nonequilibrium," *Hypersonic and High Temperature Gas Dynamics*, 2nd ed., AIAA, Reston, VA, 1989, pp. 575–598.

[2] Casseau, V., Palharini, R. C., Scanlon, T. J., and Brown, R. E., "A Two-Temperature Open-Source CFD Model for Hypersonic Reacting Flows, Part One: Zero-Dimensional Analysis," *Aerospace*, Vol. 3, No. 34, 2016, pp. 1–21. https://doi.org/10.3390/aerospace3040034

[3] Farbar, E., Boyd, I. D., and Martin, A., "Numerical Prediction of Hypersonic Flowfields Including Effects of Electron Translational Nonequilibrium," *Journal of Thermophysics and Heat Transfer*, Vol. 27, No. 4, 2013, pp. 593–606. https://doi.org/10.2514/1.T3963

[4] Casseau, V., "An Open-Source CFD Solver for Planetary Entry," Ph.D. Thesis, Dept. of Mechanical and Aerospace Engineering, Univ. of Strathclyde, Glasgow, Scotland, U.K., 2017.

[5] Koo, H., Raman, V., and Varghese, P. L., "Direct Numerical Simulation of Supersonic Combustion with Thermal Nonequilibrium," *Proceedings of the Combustion Institute*, Vol. 35, No. 2, 2015, pp. 2145–2153. https://doi.org/10.1016/j.proci.2014.08.005

[6] Fiévet, R., Voelkel, S., Koo, H., Raman, V., and Varghese, P. L., "Effect of Thermal Nonequilibrium on Ignition in Scramjet Combustors," *Proceedings of the Combustion Institute*, Vol. 36, No. 2, 2017, pp. 2901–2910. https://doi.org/10.1016/j.proci.2016.08.066

[7] Han, S., Lee, S., and Lee, B. J., "Numerical Analysis of Thermochemical Nonequilibrium Flows in a Model Scramjet Engine," *Energies*, Vol. 13, No. 3, 2020, pp. 606–623. https://doi.org/10.3390/en13030606

[8] Landsberg, W. O., Wheatley, V., Smart, M. K., and Veeraragavan, A., "Enhanced Supersonic Combustion Targeting Combustor Length Reduction in a Mach 12 Scramjet," *AIAA Journal*, Vol. 56, No. 10, 2019, pp. 3802–3807. https://doi.org/10.2514/1.J057417

[9] Barth, J. E., "Mixing and Combustion Enhancement in a Mach 12 Shape-Transitioning Scramjet Engine," Ph.D. Thesis, School of Mechanical and Mining Engineering, Univ. of Queensland, Brisbane, Australia, 2014.

[10] Dylan, J. W., and Michael, K. S., "Experimental Investigation of a Three-Dimensional Scramjet Engine at Mach 12," AIAA Paper 2015-3650, July 2015. https://doi.org/10.2514/6.2015-3650

[11] Piomelli, U., "Large-Eddy and Direct Simulation of Turbulent Flows," *Introduction to Turbulence Modelling*, Von Karman Inst., Sint-Genesius-Rode, Belgium, 2018.

[12] Sankaran, V., Genin, F., and Menon, S., "Subgrid Mixing Modeling for Large Eddy Simulation of Supersonic Combustion," AIAA Paper 2004-0801, Jan. 2004. https://doi.org/10.2514/6.2004-801

[13] Fureby, C., "LES for Supersonic Combustion," *18th AIAA/3AF International Space Planes and Hypersonic Systems and Technologies Conference*, AIAA Paper 2012-5979, 2012.

[14] Triantafyllidis, A., and Mastorakos, E., "Implementation Issues of the Conditional Moment Closure Model in Large Eddy Simulations," *Flow Turbulence Combustion*, Vol. 84, May 2009, pp. 481–512.

[15] Park, C., "The Limits of Two-Temperature Model," AIAA Paper 2010-0911, Jan. 2010. https://doi.org/10.2514/6.2010-911

[16] Park, C., "Assessment of a Two-Temperature Kinetic Model for Dissociating and Weakly Ionizing Nitrogen," *Journal of Thermophysics and Heat Transfer*, Vol. 2, No. 1, 1988, pp. 8–16. https://doi.org/10.2514/3.55

[17] Landau, L., and Teller, E., "On the Theory of Sound Dispersion," *Collected Papers of L.D. Landau*. Pergamon Press, Oxford, 1965, pp. 147–153.

[18] Millikan, R. C., and White, D. R., "Systematics of Vibrational Relaxation," *Journal of Chemical Physics*, Vol. 39, No. 12, 1963, pp. 3209–3213. https://doi.org/10.1063/1.1734182

[19] Knab, O., Fruehauf, H. H., and Messerschmid, E. W., "Theory and Validation of the Physically Consistent Coupled Vibration-Chemistry-Vibration Model," *Journal of Thermophysics and Heat Transfer*, Vol. 9, No. 2, 1995, pp. 219–226. https://doi.org/10.2514/3.649

[20] Candler, G. V., and MacCormack, R. W., "The Computation of Hypersonic Ionized Flows in Chemical and Thermal Nonequlibrium," AIAA Paper 1988-0511, Jan. 1988. https://doi.org/10.2514/6.1988-511

[21] Park, C., *Nonequilibrium Hypersonic Aerothermodynamics*, Wiley, New York, 1990.

[22] Sharma, S. P., Huo, W. M., and Park, C., "Rate Parameters for Coupled Vibration-Dissociation in a Generalized SSH Approximation," *Journal of Thermophysics and Heat Transfer*, Vol. 6, No. 1, 1992, pp. 9–21. https://doi.org/10.2514/3.312

[23] Gnoffo, P. A., Gupta, R. N., and Shinn, J. L., "Conservation Equations and Physical Models for Hypersonic Air Flows in Thermal and Chemical Nonequilibrium," NASA TP-2867, Feb. 1989.
[24] Schwer, D. A., Lu, P., and Green, W. H., "An Adaptive Chemistry Approach to Modeling Complex Kinetics in Reacting Flows," *Combustion and Flame*, Vol. 133, No. 4, 2003, pp. 451–465. https://doi.org/10.1016/s0010-2180(03)00045-2
[25] Liang, L., Stevens, J. G., and Farrell, J. T., "A Dynamic Adaptive Chemistry Scheme for Reactive Flow Computations," *Proceedings of the Combustion Institute*, Vol. 32, No. 1, 2009, pp. 527–534. https://doi.org/10.1016/j.proci.2008.05.073
[26] Zhou, D., Tay, K. L., Li, H., and Yang, W., "Computational Acceleration of Multi-Dimensional Reactive Flow Modelling Using Diesel/Biodiesel/Jet-Fuel Surrogate Mechanisms via a Clustered Dynamic Adaptive Chemistry Method," *Combustion and Flame*, Vol. 196, June 2018, pp. 197–209. https://doi.org/10.1016/j.combustflame.2018.06.008
[27] Lu, T., and Law, C. K., "A Directed Relation Graph Method for Mechanism Reduction," *Proceedings of the Combustion Institute*, Vol. 30, No. 1, 2005, pp. 1333–1341. https://doi.org/10.1016/j.proci.2004.08.145
[28] Pepiot-Desjardins, P., and Pitsch, H., "An Efficient Error-Propagation-Based Reduction Method for Large Chemical Kinetic Mechanisms," *Combustion and Flame*, Vol. 154, Nos. 1–2, 2008, pp. 67–81. https://doi.org/10.1016/j.combustflame.2007.10.020
[29] Pope, S. B., "Computationally Efficient Implementation of Combustion Chemistry Using In Situ Adaptive Tabulation," *Combustion Theory and Modeling*, Vol. 1, No. 1, 1997, pp. 41–63. https://doi.org/10.1080/713665229
[30] Yang, B., and Pope, S. B., "Treating Chemistry in Combustion with Detailed Mechanisms—In Situ Adaptive Tabulation in Principal Directions—Premixed Combustion," *Combustion and Flame*, Vol. 112, Nos. 1–2, 1998, pp. 85–112. https://doi.org/10.1016/S0010-2180(97)81759-2
[31] Lu, L., Lantz, S. R., Ren, Z., and Pope, S. B., "Computationally Efficient Implementation of Combustion Chemistry in Parallel PDF Calculations," *Journal of Computational Physics*, Vol. 228, No. 15, 2009, pp. 5490–5525. https://doi.org/10.1016/j.jcp.2009.04.037
[32] Yuan, Y., Zhang, T., Yao, W., and Fan, X., "Characterization of Flame Stabilization Modes in an Ethylene-Fueled Supersonic Combustor Using Time-Resolved Ch* Chemiluminescence," *Proceedings of the Combustion Institute*, Vol. 36, 2017, pp. 2919–2925. https://doi.org/10.1016/j.proci.2016.07.040
[33] Yao, W., and Fan, X., "Development of Zone Flamelet Model for Scramjet Combustor Modeling," AIAA Paper 2017-2277, March 2017. https://doi.org/10.2514/6.2017-2277
[34] Yao, W., and Li, B., "Application of Dynamic Zone Flamelet Model to a GH2/GO2 Rocket Combustor," AIAA Paper 2019-3868, Aug. 2019. https://doi.org/10.2514/6.2019-3868
[35] Yao, W., Liu, H., Xue, L., and Xiao, Y., "Performance Analysis of a Strut-Aided Hypersonic Scramjet by Full-Scale IDDES Modeling," *Aerospace Science and Technology*, Vol. 117, July 2021, pp. 1–14. https://doi.org/10.1016/j.ast.2021.106941
[36] Yao, W., "On the Application of Dynamic Zone Flamelet Model to Large Eddy Simulation of Supersonic Hydrogen Flame," *International Journal of Hydrogen Energy*, Vol. 45, No. 41, 2020, pp. 21940–21955. https://doi.org/10.1016/j.ijhydene.2020.05.189
[37] Pitsch, H., Wan, Y. P., and Peters, N., "Numerical Investigation of Soot Formation and Oxidation Under Diesel Engine Conditions," *Fuels & Lubricants Meeting & Exposition*, SAE TP 952357, Oct. 1995. https://doi.org/10.4271/952357
[38] Klimenko, A. Y., "On the Relation Between the Conditional Moment Closure and Unsteady Flamelets," *Combustion Theory and Modelling*, Vol. 5, No. 3, 2001, pp. 275–294. https://doi.org/10.1088/1364-7830/5/3/302
[39] Drozda, T. G., Quinlan, J. R., and Drummond, J. P., "Flamelet Modeling for Supersonic Combustion," *Modeling and Simulation of Turbulent Mixing and Reaction, Heat and Mass Transfer*, Springer, Singapore, 2020, pp. 127–168.
[40] Ladeinde, F., and Lou, Z., "Improved Flamelet Modeling of Supersonic Combustion," *Journal of Propulsion and Power*, Vol. 34, No. 3, 2018, pp. 750–761. https://doi.org/10.2514/1.B36779
[41] Gao, Z., Jiang, C., and Lee, C.-H., "Representative Interactive Flamelet Model and Flamelet/Progress Variable Model for Supersonic Combustion Flows," *Proceedings of the Combustion Institute*, Vol. 36, No. 2, 2017, pp. 2937–2946. https://doi.org/10.1016/j.proci.2016.06.184
[42] Saghafian, A., Shunn, L., Philips, D. A., and Ham, F., "Large Eddy Simulations of the Hifire Scramjet Using a Compressible Flamelet/Progress Variable Approach," *Proceedings of the Combustion Institute*, Vol. 35, No. 2, 2015, pp. 2163–2172. https://doi.org/10.1016/j.proci.2014.10.004
[43] Terrapon, V. E., Ham, F., Pecnik, R., and Pitsch, H., "A Flamelet-Based Model for Supersonic Combustion," *62nd Annual Meeting of the APS Division of Fluid Dynamics*, APS 09, American Physical Soc., Nov. 2009.
[44] Zhao, G.-Y., Sun, M.-B., Wu, J.-S., and Wang, H.-B., "A Flamelet Model for Supersonic Non-Premixed Combustion with Pressure Variation," *Modern Physics Letters B*, Vol. 29, No. 21, 2015, Paper 1550117. https://doi.org/10.1142/S0217984915501171
[45] Bilger, R. W., "Conditional Moment Closure Modelling and Advanced Laser Measurements," *Turbulence and Molecular Processes in Combustion*, Elsevier, Tokyo, Oct. 1992, pp. 267–287.
[46] Cha, C. M., and Pitsch, H., "Higher-Order Conditional Moment Closure Modelling of Local Extinction and Reignition in Turbulent Combustion," *Combustion Theory and Modeling*, Vol. 6, April 2002, pp. 425–437. https://doi.org/10.1088/1364-7830/6/3/303
[47] Kronenburg, A., and Papoutsakis, A. E., "Conditional Moment Closure Modeling of Extinction and Re-Ignition in Turbulent Non-Premixed Flames," *Proceedings of the Combustion Institute*, Vol. 30, No. 1, 2005, pp. 759–766. https://doi.org/10.1016/j.proci.2004.08.235
[48] Bilger, R. W., Starner, S. H., and Kee, R. J., "On Reduced Mechanisms for Methane-Air Combustion in Non-Premixed Flames," *Combustion and Flame*, Vol. 80, No. 2, 1990, pp. 135–149. https://doi.org/10.1016/0010-2180(90)90122-8
[49] O'Brien, E. E., and Jiang, T.-L., "The Conditional Dissipation Rate of an Initially Binary Scalar in Homogeneous Turbulence," *Physics of Fluids*, Vol. 3, No. 12, 1991, pp. 3121–3123. https://doi.org/10.1063/1.858127
[50] Pierce, C. D., and Moin, P., "A Dynamic Model for Subgrid-Scale Variance and Dissipation Rate of a Conserved Scalar," *Physics of Fluids*, Vol. 10, No. 12, 1998, pp. 3041–3044. https://doi.org/10.1063/1.869832
[51] Zhang, H., Garmory, A., Cavaliere, D. E., and Mastorakos, E., "Large Eddy Simulation/Conditional Moment Closure Modeling of Swirl-Stabilized Non-Premixed Flames with Local Extinction," *Proceedings of the Combustion Institute*, Vol. 35, No. 2, 2015, pp. 1167–1174. https://doi.org/10.1016/j.proci.2014.05.052
[52] Thornber, B., Bilger, R. W., Masri, A. R., and Hawkes, E. R., "An Algorithm for LES of Premixed Compressible Flows Using the Conditional Moment Closure Model," *Journal of Computational Physics*, Vol. 230, No. 20, 2011, pp. 7687–7705. https://doi.org/10.1016/j.jcp.2011.06.024
[53] Yao, W., and Chen, L., "Large Eddy Simulation of Rest Hypersonic Combustor Based on Dynamic Zone Flamelet Model," AIAA Paper 2020-3722, Aug. 2020. https://doi.org/10.2514/6.2020-3722
[54] Weller, H. G., Tabor, G., Jasak, H., and Fureby, C., "A Tensorial Approach to CFD Using Object Oriented Techniques," *Computers in Physics*, Vol. 12, No. 6, 1997, pp. 620–631. https://doi.org/10.1063/1.168744
[55] Lee, Y., Yao, W., and Fan, X., "Low-Dissipative Hybrid Compressible Solver Designed for Large Eddy Simulation of Supersonic Turbulent Flows," *AIAA Journal*, Vol. 56, No. 8, 2018, pp. 3086–3096. https://doi.org/10.2514/1.J056404
[56] Chen, S.-S., Yan, C., and Xiang, X.-H., "Effective Low-Mach Number Improvement for Upwind Schemes," *Computers & Mathematics with Applications*, Vol. 75, No. 10, 2018, pp. 3737–3755. https://doi.org/10.1016/j.camwa.2018.02.028
[57] Greenshields, C. J., Weller, H. G., Gasparini, L., and Reese, J. M., "Implementation of Semi-Discrete, Non-Staggered Central Schemes in a Colocated, Polyhedral, Finite Volume Framework, for High-Speed Viscous Flows," *International Journal for Numerical Methods in Fluids*, Vol. 38, No. 2, 2009, pp. 139–161. https://doi.org/10.1002/fld.2069
[58] Yao, W., Wang, J., Lu, Y., Li, X., and Fan, X., "Full-Scale Detached Eddy Simulation of Kerosene Fueled Scramjet Combustor Based on Skeletal Mechanism," AIAA Paper 2015-3579, July 2015. https://doi.org/10.2514/6.2015-3579
[59] Wu, K., Zhang, P., Yao, W., and Fan, X., "Numerical Investigation on Flame Stabilization in DLR Hydrogen Supersonic Combustor with Strut Injection," *Combustion Science and Technology*, Vol. 189, No. 12, 2017, pp. 2154–2179. https://doi.org/10.1080/00102202.2017.1365847
[60] Wu, K., Yao, W., and Fan, X., "Development and Fidelity Evaluation of a Skeletal Ethylene Mechanism Under Scramjet-Relevant Conditions,"

Energy & Fuels, Vol. 31, No. 12, 2017, pp. 14,296–14,305. https://doi.org/10.1021/acs.energyfuels.7b03033

[61] Yao, W., Lu, Y., Wu, K., Wang, J., and Fan, X., "Modeling Analysis of an Actively-Cooled Scramjet Combustor Under Different Kerosene/Air Ratios," *Journal of Propulsion and Power*, Vol. 34, No. 4, 2018, pp. 975–991. https://doi.org/10.2514/1.B36866

[62] Yao, W., Wu, K., and Fan, X., "Influences of Domain Symmetry on Supersonic Combustion Modeling," *Journal of Propulsion and Power*, Vol. 35, No. 2, 2019, pp. 451–465. https://doi.org/10.2514/1.B37227

[63] Liu, H., and Yao, W., "LES Investigation of Nonequilibrium Flow in a Cavity-Flameholding Axisymmetric Scramjet," AIAA Paper 2021-3536, Aug. 2021. https://doi.org/10.2514/6.2021-3536

[64] Zhang, Z., Yao, W., and Zhao, W., "LES Modeling of Duo-Model Scramjet by Dynamic Zone Flamelet Model," AIAA Paper 2021-3537, Aug. 2021. https://doi.org/10.2514/6.2021-3537

[65] Sun, W., Liu, H., Li, L., and Yao, W., "Large Eddy Simulation of Axisymmetric Scramjet Based on Dynamic Zone Flamelet Model," P00150, Nov. 2021.

[66] Yao, W., Liu, H., Li, L., and Yue, L., "Nonequilibrium Effect Modeling in High-Ma Scramjet Based on Dynamic Zone Model," AIAA Paper 2021-3543, Aug. 2021. https://doi.org/10.2514/6.2021-3543

[67] Wu, K., Contino, F., Yao, W., and Fan, X., "On the Application of Tabulated Dynamic Adaptive Chemistry in Ethylene-Fueled Supersonic Combustion," *Combustion and Flame*, Vol. 197, Aug. 2018, pp. 265–275. https://doi.org/10.1016/j.combustflame.2018.08.012

[68] Yao, W., "Soot Modeling in Laminar and Turbulent Combustions," Ph.D. Thesis, School of Built and Environment, Univ. of Ulster, Northern Ireland, U.K., 2010.

[69] "Ansys Fluent Theory Guide," ANSYS, Inc., Release 15.0, Canonsburg, PA, 2013.

[70] Garbaruk, M. S. G. A. V., Schütze, J., and Menter, F. R., "Development of DDES and IDDES Formulations for the K-Ω Shear Stress Transport Model," *Flow Turbulence and Combustion*, Vol. 3, Oct. 2011, pp. 1–19. https://doi.org/10.1007/s10494-011-9378-4

[71] Kee, R. J., Rupley, F. M., and Miller, J. A., "CHEMKIN-II: A Fortran Chemical Kinetics Package for the Analysis of Gas-Phase Chemical Kinetics," Sandia National Lab. Rept. SAND-89-8009, Livermore, CA, Sept. 1989.

[72] Cecere, D., and Giacomazzi, E., "An Immersed Volume Method for Large Eddy Simulation of Compressible Flows Using a Staggered-Grid Approach," *Computer Methods in Applied Mechanics and Engineering*, Vol. 280, July 2014, pp. 1–27. https://doi.org/10.1016/j.cma.2014.07.018

[73] Clarke, D. K., Hassan, H. A., and Salas, M. D., "Euler Calculations for Multielement Airfoils Using Cartesian Grids," *AIAA Journal*, Vol. 24, No. 3, 1986, pp. 353–358. https://doi.org/10.2514/3.9273

[74] Jachimowski, C. J., "An Analysis of Combustion Studies in Shock Expansion Tunnels and Reflected Shock Tunnels," NASA TP 3224, July 1992.

[75] Hassan, B., Candler, G. V., and Olynick, D. R., "Thermo-Chemical Nonequilibrium Effects on the Aerothermodynamics of Aerobraking Vehicles," *Journal of Spacecraft and Rockets*, Vol. 30, No. 6, 1993, pp. 647–655. https://doi.org/10.2514/3.26369

[76] Hash, D., Olejniczak, J., Wright, M., Prabhu, D., Pulsonetti, M., Hollis, B., Gnoffo, P., Barnhardt, M., Nompelis, I., and Candler, G., "FIRE II Calculations for Hypersonic Nonequilibrium Aerothermodynamics Code Verification: DPLR, Laura, and US3D," AIAA Paper 2007-0605, Jan. 2007. https://doi.org/10.2514/6.2007-605

[77] Park, C., "Review of Chemical-Kinetic Problems of Future NASA Missions. I—Earth Entries," *Journal of Thermophysics and Heat Transfer*, Vol. 7, No. 3, 1993, pp. 385–398. https://doi.org/10.2514/3.431

[78] Park, C., Jaffe, R. L., and Partridge, H., "Chemical-Kinetic Parameters of Hyperbolic Earth Entry," *Journal of Thermophysics and Heat Transfer*, Vol. 15, No. 1, 2001, pp. 76–90. https://doi.org/10.2514/2.6582

[79] Blottner, F. G., Johnson, M., and Ellis, M., "Chemically Reacting Viscous Flow Program for Multi-Component Gas Mixtures," Sandia Lab. Rept. SC-RR-70-754, Albuquerque, NM, Dec. 1971.

[80] Vincenti, W. G., and Kruger, C. H., *Introduction to Physical Gas Dynamics*, Krieger, New York, 1975.

[81] Gupta, R. N., Lee, K.-P., Thompson, R. A., and Yos, J. M., "Calculations and Curve Fits of Thermodynamics and Transport Properties for Equilibrium Air to 30000 K," NASA RP 1260, Oct. 1991.

[82] Bird, R. B., Stewart, W. E., and Lightfoot, E. N., "Viscosity and the Mechanisms of Momentum Transport," *Transport Phenomena*, 2nd ed., Wiley, New York, 2002, p. 27.

[83] Wilke, C. R., "A Viscosity Equation for Gas Mixtures," *Journal of Chemical Physics*, Vol. 18, No. 4, 1950, pp. 517–519. https://doi.org/10.1063/1.1747673

[84] Liu, I.-S., "On Fourier's Law of Heat Conduction," *Continuum Mechanics and Thermodynamics*, Vol. 2, Dec. 1990, pp. 301–305. https://doi.org/10.1007/BF01129123

[85] Sutton, K., and Gnoffo, P., "Multi-Component Diffusion with Application to Computational Aerothermodynamics," *7th AIAA/ASME Joint Thermophysics and Heat Transfer Conference*, AIAA Paper 1998-2575, June 1998. https://doi.org/10.2514/6.1998-2575

[86] Kurganov, A., Noelle, S., and Petrova, G., "Semidiscrete Central-Upwind Schemes for Hyperbolic Conservation Laws and Hamilton-Jacobi Equations," *SIAM Journal on Scientific Computing*, Vol. 23, No. 3, 2001, pp. 707–740. https://doi.org/10.1137/S1064827500373413

[87] Pirozzoli, S., "Generalized Conservative Approximations of Split Convective Derivative Operators," *Journal of Computational Physics*, Vol. 229, No. 19, 2010, pp. 7180–7190. https://doi.org/10.1016/j.jcp.2010.06.006

[88] Vuorinen, V., Larmi, M., Schlatter, P., Fuchs, L., and Boersma, B. J., "A Low-Dissipative, Scale-Selective Discretization Scheme for the Navier–Stokes Equations," *Computers & Fluids*, Vol. 70, Sept. 2012, pp. 195–205. https://doi.org/10.1016/j.compfluid.2012.09.022

[89] Crank, J., and Nicotson, P., "A Practical Method for Numerical Evaluation of Solutions of Partial Differential Equations of the Heat-Conduction Type," *Advances in Computational Mathematics*, Vol. 6, Dec. 1996, pp. 207–226. https://doi.org/10.1007/BF02127704

[90] Delichatsios, M. A., "Transition from Momentum to Buoyancy-Controlled Turbulent Jet Diffusion Flames and Flame Height Relationships," *Combustion and Flame*, Vol. 92, No. 4, 1993, pp. 349–364. https://doi.org/10.1016/0010-2180(93)90148-V

[91] Goussis, D. A., Im, H. G., Najm, H. N., Paolucci, S., and Valorani, M., "The Origin of CEMA and Its Relation to CSP," *Combustion and Flame*, Vol. 227, Jan. 2021, pp. 396–401. https://doi.org/10.1016/j.combustflame.2021.01.020

[92] Lu, T. F., Yoo, C. S., Chen, J. H., and Law, C. K., "Three-Dimensional Direct Numerical Simulation of a Turbulent Lifted Hydrogen Jet Flame in Heated Coflow: A Chemical Explosive Mode Analysis," *Journal of Fluid Mechanics*, Vol. 652, Jan. 2010, pp. 45–64. https://doi.org/10.1017/s002211201000039x

[93] Odam, J., and Paull, A., "Radical Farming in Scramjets," *New Results in Numerical and Experimental Fluid Mechanics VI*, Springer, Berlin, 2007, pp. 276–283.

[94] Eitelberg, G., "First Results of Calibration and Use of the HEG," AIAA Paper 1994-2525, June 1994. https://doi.org/10.2514/6.1994-2525

[95] Hornung, H. G., "28th Lanchester Memorial Lecture—Experimental Real-Gas Hypersonics," *Aeronautical Journal*, Vol. 92, No. 920, 2016, pp. 379–389. https://doi.org/10.1017/s0001924000016511

[96] Smart, M. K., "How Much Compression Should a Scramjet Inlet Do?" *AIAA Journal*, Vol. 50, No. 3, 2012, pp. 610–619. https://doi.org/10.2514/1.j051281

[97] Li, B., Yao, W., Lee, Y., and Fan, X., "Reconstruction Model for Heat Release Rate Based on Artificial Neural Network," *International Journal of Hydrogen Energy*, Vol. 46, No. 37, 2021, pp. 19,599–19,616. https://doi.org/10.1016/j.ijhydene.2021.03.074

[98] Law, C. K., "Theories of Reaction Rates: Basic Concepts," *Combustion Physics*, Cambridge Univ. Press, Cambridge, England, U.K., 2006, p. 58.

[99] Borghi, R., "Turbulent Combustion Modelling," *Progress in Energy and Combustion Science*, Vol. 14, No. 4, 1988, pp. 245–292. https://doi.org/10.1016/0360-1285(88)90015-9

[100] Pope, S. B., "Ten Questions Concerning the Large-Eddy Simulation of Turbulent Flows," *New Journal of Physics*, Vol. 6, March 2004, pp. 35–35. https://doi.org/10.1088/1367-2630/6/1/035

[101] Ingenito, A., and Bruno, C., "Physics and Regimes of Supersonic Combustion," *AIAA Journal*, Vol. 48, No. 3, 2010, pp. 515–525. https://doi.org/10.2514/1.43652

[102] Villasenor, R., Pitz, R. W., and Chen, J. Y., "Interaction Between Chemical Reaction and Turbulence in Supersonic Nonpremixed H2-Air Combustion," *29th Aerospace Sciences Meeting*, AIAA Paper 1991-0375, Jan. 1991. https://doi.org/10.2514/6.1991-375

[103] Yao, W., Wu, K., and Fan, X., "Development of Skeletal Kerosene Mechanisms and Application to Supersonic Combustion," *Energy & Fuels*, Vol. 32, No. 12, 2018, pp. 12,992–13,003. https://doi.org/10.1021/acs.energyfuels.8b03350

J. C. Oefelein
Associate Editor